

Numerical simulations of ICME–ICME interactions

Tatiana Niembro^{1,2,*}, Alejandro Lara², Ricardo Francisco González³, and Jorge Cantó⁴

¹ Posgrado en Ciencias de la Tierra, Universidad Nacional Autónoma de México, CDMX, 04510, México

² Instituto de Geofísica, Universidad Nacional Autónoma de México, Ciudad Universitaria, CDMX, 04510, México

³ Instituto de Radioastronomía y Astrofísica, Universidad Nacional Autónoma de México, Apdo. Postal 3-72, Morelia, Michoacán, 58089, Mexico

⁴ Instituto de Astronomía, Universidad Nacional Autónoma de México, Ciudad Universitaria Apdo. Postal 70-264, CDMX, 04510, México

Received 20 July 2018 / Accepted 3 December 2018

Abstract – We present hydrodynamical simulations of the interaction of Coronal Mass Ejections (CME) in the Interplanetary Medium (IPM). In these events, two consecutive CMEs are launched from the Sun in similar directions within an interval of time of a few hours. In our numerical model, we assume that the ambient solar wind is characterized by its velocity and mass-loss rate. Then, the CMEs are generated when the flow velocity and mass-loss rate suddenly change, with respect to the ambient solar wind conditions during two intervals of time, which correspond to the duration of each CME. After their interaction, a merged region is formed and evolve as a single structure into the IPM. In this work, we are interested in the general morphology of this merged region, which depends on the initial parameters of the ambient solar wind and the CMEs involved. In order to understand this morphology, we have performed a parametric study in which we characterize the effects of the initial parameters variations on the density and velocity profiles at 1 AU, using as reference the well-documented event of July 25th, 2004. Based on this parametrization we were able to reproduce the main features of the observed profiles ensuring the travel time and the speed and density magnitudes. Then, we apply the parametrization results to the interaction events of May 23, 2010; August 1, 2010; and November 9, 2012. With this approach and varying the values of the input parameters within the CME observational errors, our simulated profiles reproduce the main features observed at 1 AU. Even though we do not take into account the magnetic field, our models give a physical insight into the propagation and interaction of ICMEs.

Keywords: Hydrodynamics / shock waves / Sun: activity / Sun: coronal mass ejections (CMEs) / solar wind

1 Introduction

Coronal Mass Ejections (CMEs) are powerful solar eruptions that release huge amount of mass into the Interplanetary Medium (IPM). Their masses can be as large as 10^{15} – 10^{16} g moving outwards at speeds ranging from a few hundreds to thousands kilometers per second (Strong et al., 1999). Interaction of these eruptions with the solar wind lead to the formation of shock waves that travel through the IPM (Pizzo, 1985). Several authors have investigated the CME propagation through the inner heliosphere (Sun-to-Earth), which is a fundamental issue in space weather forecasting (e.g., Vršnak, 2001; Borgazzi et al., 2009; Liu et al., 2013; Gopalswamy, 2016). On the other hand, few authors have addressed the dynamics of interacting events (Liu et al., 2012; Temmer et al., 2012).

In such cases, two consecutive CMEs launched from the Sun in similar directions collide and the resulting merged structure continues the propagation interacting with the ambient solar wind (Burlaga et al., 2002, 2003). Based on the rate of CME production (Gopalswamy et al., 2001; Yashiro et al., 2004) and their typical propagation times (3–4 days) to 1 AU, one can assume that there may be from 2 to 20 CMEs in the 4π sr between the Sun and the Earth (Lugaz et al., 2017), enabling the CME–CME interaction to occur usually, more frequently during the maximum of the solar cycle. Furthermore, the difficulty of unambiguously determine the arrival of a complex structure from *in situ* data (Burlaga et al., 2003), may be explained by the possibility that some of these structures were formed by the interaction of two or more CMEs. This may be the main cause the failure in the models that attempt to predict the travel time of a single CME. Thus, it is important to study both the CME propagation through the IPM and the dynamics of the ICME–ICME interaction events. The physics of these

*Corresponding author: tatiana@igeofisica.unam.mx

phenomena is not yet well understood, and hence, it is still one of the goals for space research.

The detection of CMEs near the Sun can be achieved by coronagraphic observations, while their counterparts ICMEs can be detected by multi-spacecraft *in situ* measurements. Consequently, the identification of CME–ICME corresponding pairs is difficult (Lara et al., 2006), just in a very few cases, it has been possible to track ICMEs from the Sun to the Earth by using the STEREO heliospheric imager (see, for instance, Harrison et al., 2012; Lugaz et al., 2012; Temmer et al., 2012) but the analysis of these images is not enough to fully understand the physics behind their evolution.

From a theoretical point of view, both, analytical and numerical models have been developed for a better understanding of the ICMEs dynamical evolution, propagation and possible interaction among these structures.

Analytically, several models have been developed (e.g., Chen, 1996; Vršnak, 2001; Borgazzi et al., 2009; Vršnak et al., 2013, 2014) in which the CME is described as an amount of mass and magnetic field that is expelled out to the IPM with velocity different than the solar wind. Near the Sun, the CME dynamics is governed by the gravity, the Lorentz force and the aerodynamic drag. However, in the interplanetary medium (above $20 R_{\odot}$), the gravity, and the Lorentz force contributions can be assumed negligible, meaning that the ICME kinematics depends on the ICME and the ambient solar wind conditions (speed and density) and a dimensionless drag coefficient (e.g., Vršnak & Gopalswamy, 2002; Vršnak et al., 2004, 2010). In the same direction, Cantó et al. (2005) developed a model to describe the CMEs evolution. In this model, the Sun is continuously expelling out solar wind with constant mass-loss rate (\dot{m}_{SW} ; the mass density at the base of the wind is ρ_{SW}) and speed (v_{SW}). Suddenly at the CME injection point ($R \approx 20 R_{\odot}$), the conditions of the flow are perturbed, assuming that the CME is the perturbation in which the speed and density abruptly changes by constant factors a and c , respectively. The injection velocity changes from v_{SW} to $a v_{\text{SW}}$ and the density from ρ_{SW} to $c \rho_{\text{SW}}$ for an interval of time Δt . The mass involved in the perturbation is $m = a c \dot{m}_{\text{SW}} \Delta t$ (Cantó et al., 2005).

In terms of prediction, the results of the analytical models are very similar with errors ranging from less than 1 h to more than 8 h, depending on the event. When applied to ICME–ICME interactions, these models are used assuming that each of the interacting ICMEs travels alone and then computing the time and distance of the interaction. Afterwards, it is supposed that a merged region is formed and travels with an intermediate constant speed (up to 1 AU).

Recently, Niembro et al. (2015) have performed an analytic study of ICMEs interactions. These authors applied the formalism developed by Cantó et al. (2005), in order to study the dynamics of two consecutive CMEs launched in the same direction from the Sun. The collision yields a merged region that contains material expelled during both eruptions and propagates afterwards as a single structure. The time and the distance of the collision, as well as the travel time to 1 AU of the merged region is predicted for a set of well documented interaction events (January 24, 2007; May 23, 2010; August 1, 2010; and November 9, 2012) with errors of less than two

hours in the prediction of the collision time, less than eight hours for the travel time to 1 AU and less than 50 km s^{-1} in terms of speed. This is the first analytic model developed to describe hydro-dynamically the interaction between ICMEs. The main feature of the model is the inclusion of the modification of the solar wind conditions due to the propagation of the first ICME and the evolution of the merged region.

Any of these analytical models can predict the travel time, speed and density of the ICMEs/merged region at any heliospheric distance. Nevertheless, they cannot predict the *in situ* parameter time-profiles observed at 1 AU. This issue is one of the main purposes addressed by the numerical models presented in this work.

The physical basis for most simulations includes the gravitational, the Lorentz, and/or the aerodynamic drag forces (e.g., Chen, 1996; Cargill, 2004), pressure gradients, etc.; integrated into dynamical HD or MHD equations (e.g., González-Esparza et al., 2003; Xiong et al., 2007; Shen et al., 2011, 2013; Lugaz et al., 2013). Various models are reviewed by Zhao & Dryer (2014) and Lugaz et al. (2017). Most of the numerical models have good results about the prediction of the arrival magnitude of the velocity and density of ICMEs, although, their performance is relatively poor in terms of the time profile morphology of the *in situ* parameters (see for instance, Lugaz et al., 2008; Temmer et al., 2011; Manchester et al., 2014). Our ability to successfully model is still limited (Zhao & Dryer, 2014) and better prediction requires improvements in: (1) The uncertainties in the input parameters, (2) the knowledge of 3-D morphology and kinematics; (3) the real background solar wind; and (4) other known (deflection, reconnection, etc.) and unknown factors.

With this in mind, we focus our work in terms of the uncertainties in the input parameters. We have performed hydrodynamical simulations for a single ICME and for ICME–ICME interaction events. We carried out a parametric study of a single ICME to find out which are the most relevant quantities for the morphology of the time-dependent profile, and then to obtain the model that best match the observed density and velocity profiles varying the least the input parameters.

In our HD models, we have assumed that the propagation of any associated density enhancements – such as plasma sheath regions, shocks, solar wind pileup, or compression regions – is not affected by the magnetic field (Prise et al., 2015), so that, the travel time, speed, density, and dynamic pressure of the events are still well reproduced at 1 AU.

We have compared our results to those obtained with the aerodynamic drag force (Vršnak et al., 2010) and the MHD ENLIL model (Falkenberg et al., 2010) to demonstrate that our study is comparable to all these approaches (or any with similar physical basis), and gives reliable insights of the dynamics of a single CME as a function of the injection parameters.

This paper is organized as follows. In Section 2, we describe the numerical models. In Section 3, we present the parametric study for the dynamics of a single CME as function of the input parameters. The numerical simulations of ICME–ICME interaction events, and the discussion of the results are presented in Section 4. Finally, in Section 5 we give our conclusions.

2 The numerical models

We investigate through numerical hydrodynamical simulations the propagation of a single CME into the solar wind, as well as ICME–ICME interaction events. We focus on the ICME dynamics (macroscopic scale), assuming that the kinetic energy of the plasma is much higher and therefore dominates over the magnetic energy (see, for instance, [Borgazzi et al., 2009](#)).

The numerical simulations have been performed using an adiabatic 2D hydrodynamic version of the adaptive grid code YGUAZÚ-A, originally developed by [Raga et al. \(2000\)](#) and modified by [González et al. \(2004a, 2004b, 2010\)](#). The code integrates a system of equations consisting of the 2D Cartesian coordinate Euler equations for the atomic/ionic species HI, HII, HeI, HeII, and HeIII, with the abundances (by number) of H = 0.9 and He = 0.1.

The solar wind is assumed as a supersonic (with an initial temperature of 10^5 K) and inviscid flow which obeys the very well known conservative equations of mass, momentum, and energy, which are written in the code as follows:

$$\frac{\partial \mathbf{U}}{\partial t} + \frac{\partial \mathbf{F}}{\partial x} + \frac{\partial \mathbf{G}}{\partial y} = \mathbf{S}, \quad (1)$$

where,

$$\mathbf{U} = \begin{bmatrix} \rho \\ \rho u \\ \rho v \\ E \\ n_1 \\ n_2 \\ n_3 \\ n_4 \\ n_5 \end{bmatrix}, \quad \mathbf{F} = \begin{bmatrix} \rho u \\ P + \rho u^2 \\ \rho uv \\ u(E + P) \\ n_1 u \\ n_2 u \\ n_3 u \\ n_4 u \\ n_5 u \end{bmatrix}, \quad \mathbf{G} = \begin{bmatrix} \rho v \\ \rho uv \\ P + \rho v^2 \\ v(E + P) \\ n_1 v \\ n_2 v \\ n_3 v \\ n_4 v \\ n_5 v \end{bmatrix},$$

$$\text{and } \mathbf{S} = \begin{bmatrix} 0 \\ 0 \\ 0 \\ 0 \\ S_1 \\ S_2 \\ S_3 \\ S_4 \\ S_5 \end{bmatrix}. \quad (2)$$

where $E = \frac{1}{2}\rho(u^2 + v^2) + C_V P$ is the total gas energy, (u , v) are the speed components in the (x , y)-directions, ρ is the mass density, $P = (n_i + n_e)kT$ is the thermal pressure (with n_i and n_e the total number of ions and electrons, respectively), T is the temperature, n_1, n_2, \dots, n_5 the number of densities of HI, HII, HeI, HeII, and HeIII, respectively. $C_V = 1/(y - 1) = 1.5$ (with $y = 5/3$) is the specific heat at constant volume. The temperature T determines the state of ionization (in this case fully ionized) and then the code computes the total number of ions and electrons and the mass related to the species. Both numbers are needed for solving the energy equation. In addition, \mathbf{F} and \mathbf{G} are the fluxes in the x and y

directions, respectively, and \mathbf{S} is the source vector that includes the energy gain and energy loss to the equation.

The simulations were computed on a five-level binary adaptive grid with a maximum resolution of 1.465×10^{10} cm (0.001 AU), corresponding to 1024×1024 grid points extending over a computational domain of 1.5×10^{13} cm \times 1.5×10^{13} cm (1 AU \times 1 AU) and time steps of 15 min. This code allowed us to perform numerical simulations with better spatial resolution than those models developed with the ENLIL code (for the particular cases treated in this study), which were done with a time step of 8 min and a grid resolution of $256 \times 30 \times 90$ ([Falkenberg et al., 2010](#)).

The computational domain is filled by an isotropic flow with typical solar wind conditions (speed v_{SW} and mass-loss rate \dot{m}_{SW}). In our simulations, the central source is located at the *left-bottom* corner of the computational domain (Cartesian coordinates $[0,0]$) with a radius of $R_{\text{inj}} = 1.4 \times 10^{12}$ cm (≈ 0.09 AU). Once all the computational domain is filled. Then the CMEs are imposed as sudden changes of the flow at the injection radius R_{inj} . The CME is launched in the following way: the conditions of the flow change during an interval of time within a solid angle (which corresponds to a total angular width of ϕ) with an ejection speed v ($> v_{\text{CME}}$) and a mass-loss rate (\dot{m}_{CME}). Afterwards, the solar wind resumes (v_{SW} and \dot{m}_{SW}).

The CME is launched in the direction $\theta = 0$ and its velocity profile is defined following an angular dependence, so that:

$$V(\theta) = A + B \tanh h \left(\frac{|\theta| - \omega}{k} \right), \quad (3)$$

with,

$$A = \frac{v_{\text{CME}} + v_{\text{SW}}}{2} \text{ and } B = v_{\text{SW}} - A, \quad (4)$$

where $2\omega = \phi$ with ω the CME half angular width, and k is a constant that controls the shape of change of $V(\theta)$. With this, $v = V(\theta)$ and $\dot{m} = \rho v$. When $\theta = 0$ then we are at the nose of the CME which means maximum speed, that is, for k small enough, $V(\theta) \approx v_{\text{CME}}$ ($V(\theta) = v_{\text{CME}}$ is only achieved at the limit $k = 0$), while when $\theta = \pi/2$ then $V(\theta) \approx v_{\text{SW}}$ which is the minimum value.

As an example, in [Figure 1](#), we present snapshots of the CME simulation (with a speed $v_{\text{CME}} = 1330$ km s^{-1} , a mass-loss $\dot{m}_{\text{CME}} = 1.1 \times 10^{16}$ g during an interval of time $\Delta t = 2$ h, and an angular width $\phi = 1.8$ rad) at three different heliospheric distances: 0.18 AU, 0.48 AU, and 0.98 AU. The *upper panel* corresponds to the CME velocity profiles (shade in *gray*) while the *bottom panel* shows the CME density profiles (shade in *red*). The enhanced density is concentrated at the front of the CME while the expansion velocity profile has a much longer extension, as also shown with density and velocity profiles in [Figure 2](#). The CME expulsion is assumed to be axisymmetric with its axis of symmetry perpendicular to the direction of propagation. The solar wind conditions were taken as $v_{\text{SW}} = 650$ km s^{-1} and a mass-loss rate $\dot{m}_{\text{SW}} = 9.27 \times 10^{-15}$ $M_{\odot} \text{ yr}^{-1}$.

Close to the Sun the solar magnetic field is very strong and dominates the dynamics of the solar wind. However, at larger distances, the solar magnetic field is quite weak (the radial component decreases as the inverse of the distance squared) and thus, not far from the Sun the dynamical influence of the solar magnetic field on the dynamics of the solar wind becomes

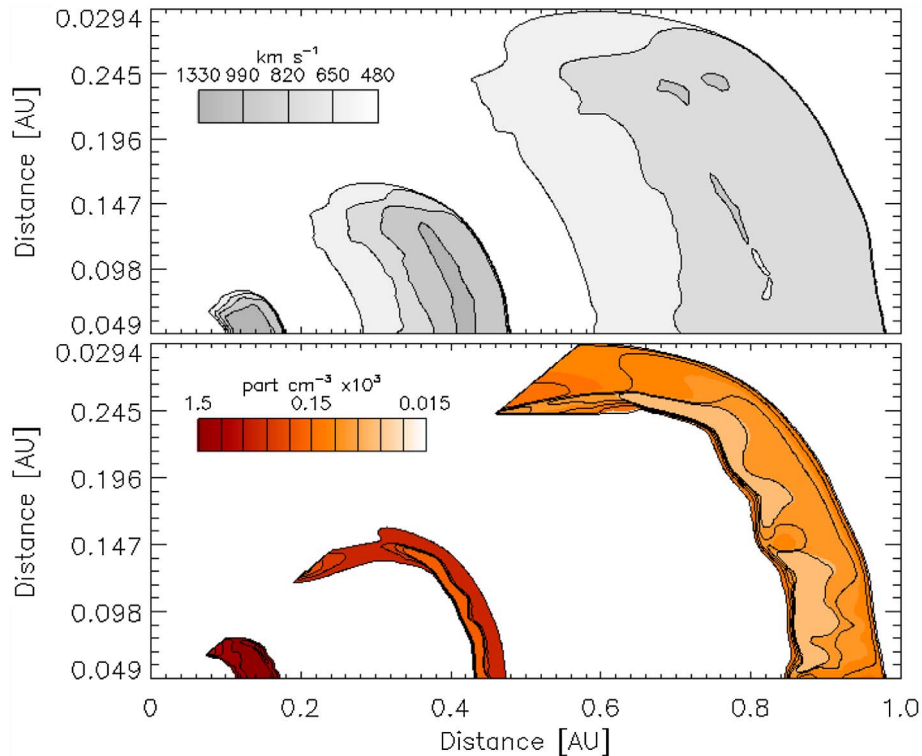


Fig. 1. Snapshots of the CME simulation at three different heliospheric distances: 0.18 AU, 0.48 AU, and 0.98 AU. The *upper panel* corresponds to the CME velocity profiles (shade in *gray*) while the *bottom panel* shows the CME density profiles (shade in *red*). The input parameters correspond to the event of July 25, 2004, studied by [Falkenberg et al. \(2010\)](#); [Vršnak et al. \(2010\)](#) and as the parametric study reference used in this work (see [Sect. 3](#)).

negligible. The injection radius was estimated as the distance at which the role of the magnetic field changes by comparing the kinetic energy of the flow with the magnetic energy and find that the Alfvénic critical point is approximately $20 R_{\odot}$ (~ 0.09 AU; [Mihalas, 1978](#)).

[Falkenberg et al. \(2010\)](#) note that despite ENLIL being unable to simulate the internal magnetic structure of the ICME, the travel time, speed, density, and dynamic pressure of the event is well reproduced at 1 AU. Furthermore, [Vršnak et al. \(2010\)](#) compare the ENLIL + cone model with the analytic drag-based model, finding that their results are similar for both models (with travel time differences of <8 h). Based on these results, in this work, we used hydro-dynamical simulations of a single ICME to carry out a parametric study and find out which are the most relevant quantities for the time profile morphology, considering: the travel time, the arrival speed and density magnitudes, the duration of the compression region and the rarefaction zone. These features are expected to be well reproduced at 1 AU by hydro-dynamical models. We compare our results with [Vršnak et al. \(2010\)](#) who in turn compared their results with those obtained by ENLIL code. Based on the parametric study, we were able to obtain the closest models to the observed density and velocity profiles during the propagation of a single ICME and three ICME–ICME interaction events, by varying the input parameters as little as possible.

By selecting those events in which the ICMEs propagation axes are very close to the Sun–Earth direction and have high speeds and large masses, we can neglect the deflection and

rotation effects due to the magnetic field ([Kay & Opher, 2015](#)). This means, that the evolution of the compression regions are dominated by the kinetic energy of the ICMEs ([Siscoe & Odstrcil, 2008](#)) and are independent of the internal magnetic field of the ICMEs ([Riley et al., 2004](#); [Owens et al., 2005](#)). Also, we assume that the *in situ* observatory is localized in the nose path of the ICME, allowing us to neglect geometry and projection effects ([Schwenn et al., 2005](#)). Deviations of these assumptions are considered limitations of our 2D model.

3 Parametric study of the dynamics of a single CME

In order to explain the time-dependent profiles of the observed *in situ* physical properties of the solar wind, we have performed a parametric study of the dynamics of a single CME as a function of the injection parameters. Taking into account that the *in situ* observed morphology of a fast ICME is characterized by a shock front, a compression region and a rarefied zone, in this section, we present a comparison between observations of the July 25, 2004 event with numerical models computed by the YGUAZÚ-A code.

3.1 Event of July 25, 2004

[Vršnak et al. \(2010\)](#) studied this event using different drag based models to investigate the CME kinematics assuming that

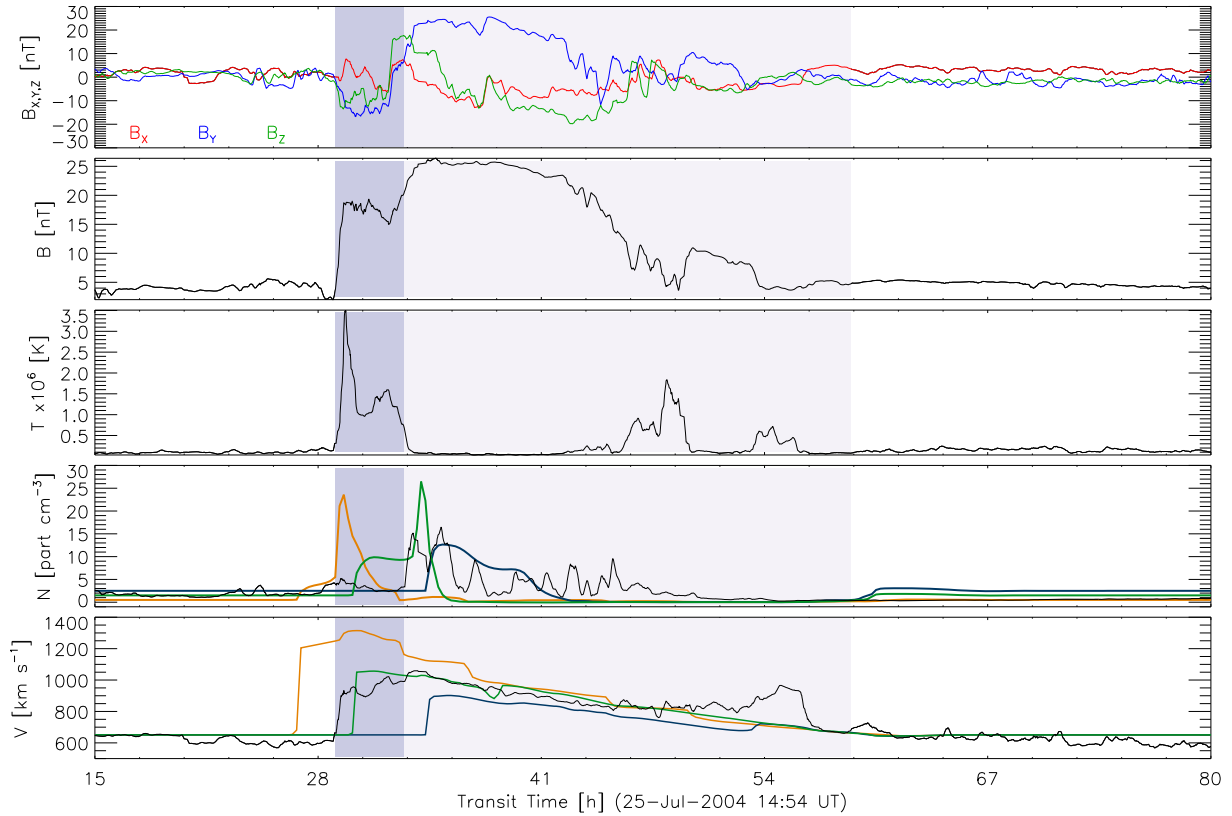


Fig. 2. WIND spacecraft measurements (from top to bottom): B_x , B_y and B_z ; B ; T ; N ; and v . In the last two panels we include the respective profiles predicted by the models listed in Table 1: MAX (in blue), MEDIUM (in green), and MIN (in amber). The model MEDIUM is the closest model to observations. The *in situ* data are shown with a smoothed time window of 15 min, which coincides with the time resolution of our simulations. In purple shades we mark the duration of the compression region and the duration of the rarefaction zone, according to the WIND ICME list (Nieves-Chinchilla et al., 2016, 2018).

Table 1. Comparison between the predicted and observed travel times and speeds at 1 AU.

	ϕ rad	n part cm ⁻³	TT h	ΔTT^a h	v km s ⁻¹	Δv^b km s ⁻¹
MAX	2.6	2.5	36.25	-3.65	888	112
MEDIUM	1.8	1.5	31.5	1.1	1033	-33
MIN	1.1	0.5	30.25	2.35	1319	-319

^a $\Delta TT = TT_{\text{obs}} - TT$, being TT_{obs} the observed transit time and TT the calculated value;

^b $\Delta v = v_{\text{obs}} - v$, where v_{obs} and v are the observed and calculated speeds at 1 AU, respectively.

the velocity, the mass loss rate and the angular width of the eruption, as well as the solar wind conditions change over time. These authors focused on the CME transit-time, density, and speed at 1 AU. To compare our numerical results with their results, we have performed three distinct simulations using the medium and extremes (minimum and maximum) values of the angular width and solar wind density adopted by these authors.

In the Sun–Earth event of July 25, 2004, a CME was detected with a speed $v = 1330$ km s⁻¹, in which a total mass $m = 1.1 \times 10^{16}$ g was expelled during an interval of time

$\Delta t = 2.0$ h within a solid angle $\Omega/4\pi$ ranging from 0.07 (which corresponds to a total angular width of $\phi = 1.1$ rad) to 0.36 ($\phi = 2.6$ rad), with these values the mass-loss rate is ranged from $3.285 \times 10^{-13} M_{\odot} \text{ yr}^{-1}$ to $6.62 \times 10^{-14} M_{\odot} \text{ yr}^{-1}$. Here, we adopt for the solar wind a terminal velocity $v_{\text{SW}} = 650$ km s⁻¹, and a number density $N = 0.5$ – 2.5 cm⁻³ at 1 AU. The corresponding ICME was observed by the WIND spacecraft at a transit time $TT_{\text{obs}} = 31.5$ h and a velocity of $v_{\text{obs}} = 1033$ km s⁻¹. All these parameters are consistent with those reported by Vršnak et al. (2010).

Table 1 shows our numerical results for the MIN, MEDIUM, and MAX models, which correspond to the minimum, medium and maximum values of ϕ and n , reported by Vršnak et al. (2010). The first column shows the corresponding CME angular widths and the second the solar wind densities at 1 AU. Third, fourth, fifth and sixth columns are the transit time TT , the difference between the observed transit time and the computed value $\Delta TT = TT_{\text{obs}} - TT$, the predicted velocity v , and the difference between the observed and calculated velocities $\Delta v = v_{\text{obs}} - v$, respectively.

In model MEDIUM, we forecast that the ICME delays 1.1 h with respect to the observed travel time, reaching the Earth with a velocity that differs only by $\Delta v = -33$ km s⁻¹ with respect to the observed 1 AU speed. The largest transit time, $TT = 36.25$ h, is obtained with model MIN, which implies a relative difference of $\Delta TT = -3.65$ h. As concerns

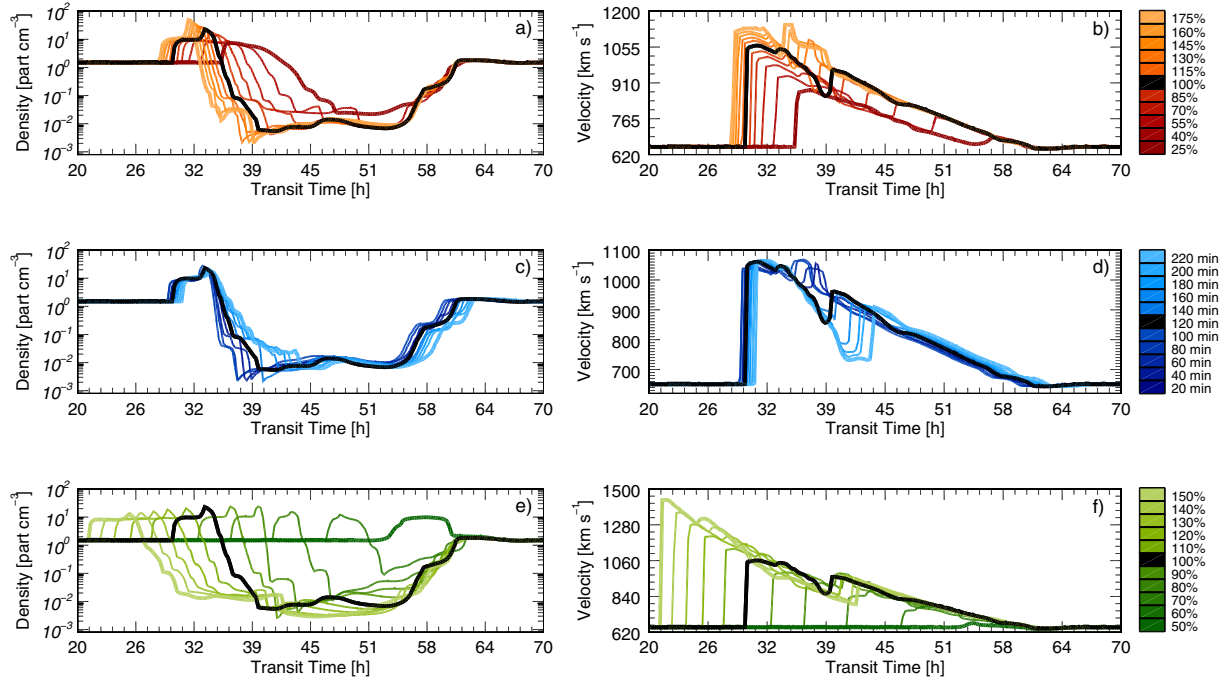


Fig. 3. Predicted density and velocity profiles as function of time for numerical models with different input parameters (expelled mass m , duration Δt , and ejection velocity V) of the CME. The models are performed varying only one parameter, and the others are fixed. *Orange* profiles (*top panels*) are obtained from variations of m ; *blue* profiles (*middle panels*) correspond to different values of Δt ; and *green* profiles (*bottom panels*) are calculated changing v . The color bars at the right side show the variation of each parameter, and the *black lines* correspond to the predicted profiles of the reference model with $m = 1.1 \times 10^{16}$ g, $\Delta t = 2.0$ h, and $v = 1330$ km s $^{-1}$). See the text for further description.

the arrival velocity, we predict that the major deviation from the observed speed is $\Delta v = -319$ km s $^{-1}$ predicted by model MAX.

Figure 2 shows a comparison of the *in situ* data, obtained by WIND in *black line* (from *top to bottom*) the components (B_X , B_Y and B_Z), and the magnitude of the magnetic field (B), the proton temperature (T), the density (N) and the velocity (V) with our models MIN, MEDIUM, and MAX depicted with *amber*, *green* and *blue lines*, respectively are presented in the last two *panels*. We mark in *purple* shades the duration of the compression region and the rarefaction zone found in the WIND ICME list (Nieves-Chinchilla et al., 2016, 2018). As seen in the figure, the shape of the predicted profiles changes considerably depending on the CME angular width and the solar wind density (shown in first and second column of Table 1, respectively). Based on these changes of the computed profiles, and to further investigate this dependence, we carried out several numerical simulations varying the initial conditions of the outflows. This parametric study may help to determine the most relevant variables for the ICME forecasting.

In order to get an insight of the ICME transport phenomena, we have varied the initial parameters of the CME and study their impact on the predicted physical properties of the corresponding ICME (travel time, speed and density magnitudes, compression region duration and the rarefaction zone duration) at 1 AU. We have adopted the July 25, 2004 event (the model MEDIUM previously described) as reference, and then, we vary one of the injection parameters while the others are fixed. Section 3.2, we present the results obtained by

computing different models changing both the CME injection parameters, and the solar wind conditions before and after the eruption (Sect. 3.3).

3.2 Numerical models assuming different parameters of the CME

The three relevant parameters of the CME modified in our analysis were: the ejection velocity v , the expelled mass m , and the duration of the eruption Δt . In this case the solar wind parameters are fixed with a speed $v_{\text{SW}} = 650$ km s $^{-1}$ and a mass-loss rate $\dot{m}_{\text{SW}} = 9.27 \times 10^{-15}$ M_{\odot} yr $^{-1}$. The reference values for the CME parameters (corresponding to the model MEDIUM described in Sect. 2) are: $v = 1330$ km s $^{-1}$, $m = 1.1 \times 10^{16}$ g, $\Delta t = 2.0$ h ($\dot{m}_{\text{CME}} = 1.28 \times 10^{-13}$) M_{\odot} yr $^{-1}$), $\phi = 1.8$ rad, and both flows (SW and CME) with a temperature $T = 10^5$ K. In this case, the CME is modeled by an increase of velocity by a factor 2 while the mass loss-rate by a factor 13.8. In Figure 3, we present the predicted density and velocity profiles at 1 AU (*left and right panels*, respectively) varying the initial parameters of the CME: the expelled mass (*top panels*), the duration of the CME (*middle panels*), and the ejection velocity (*bottom panels*). The color bars at the right side of the figure show the corresponding values for each *color line*. The *black lines* represents the reference density and velocity profiles obtained from the model MEDIUM.

We have performed 10 simulations varying $\pm 15\%$, $\pm 30\%$, $\pm 45\%$, $\pm 60\%$, and $\pm 75\%$ the reference value of m . The resulting density and velocity profiles are shown in *panels* (a) and (b)

of Figure 3, respectively. The profile in *dark-red* corresponds to the lowest mass (2.75×10^{15} g), while the profile in *light-orange* corresponds to the highest mass (1.925×10^{16} g).

We can see from density profiles that, as the expelled CME mass decreases, the compression region last for a longer time, and the transit time is longer. In addition, the density profiles show that the compression region morphology smooths (the two peaks vanished) and the rarefaction is less deep. On the other hand, the velocity profiles predicts stronger arrival shocks (higher velocity jumps) for higher mass eruptions. A second peak due to a contact discontinuity appears in the velocity profile and evolves onto the rarefaction zone. It is noticeable that this second jump is more perceptible in models with higher mass eruptions.

Furthermore, we carried out numerical simulations in which the duration of the eruption was changed. In the *middle panels* of Figure 3, we present the density and velocity profiles (*left and right*, respectively) which are predicted by ten different simulations. The adopted time variation is of ± 20 min, ranging from the minimum duration of 20 min (*dark blue*) to the maximum duration of 220 min (*light blue*). It can be seen from the figure that the adopted variations of the CME duration result in travel times of the shock structure at 1 AU that differ less than one hour among the models. We also note that the main features of the density profiles are very similar to that obtained from the reference model MEDIUM (*black line*), while the velocity profiles show a second maximum more distant behind the leading shock front as the duration of the eruption increases.

Finally, we computed 10 more simulations varying the injection velocity of the CME by $\pm 10\%$, $\pm 20\%$, $\pm 30\%$, $\pm 40\%$, and $\pm 50\%$, with respect to the model MEDIUM. In Figure 3 (*bottom panels*), the predicted density and velocity profiles are presented. The *darkest green* represents a model with an injection velocity of 665 km s^{-1} , while the *lighter one* corresponds to a model with an initial speed of 1995 km s^{-1} . As expected, it is shown that the travel time to 1 AU is shorter as the CME velocity increases. In addition, it can be seen from the density profiles that the detection of the compression region, and the corresponding rarefaction zone as well, last for longer times in higher speed models. The transition between both regions becomes steeper for lower injection velocities. We also note that deeper and more extended low-density regions are produced behind the shock wave as the injection velocity of the CME increases.

As it can be seen in Figure 3, it is remarkable the dependence of the model results with the remote sensing observations. In particular, variations of the injection velocity of the CME produce the major changes in the predicted density and velocity profiles. Nonetheless, one cannot arbitrarily change this parameter as the estimation of the measured velocity has the lowest observational error of $\pm 20 \text{ km s}^{-1}$ (Yashiro et al., 2004; Xie et al., 2004). On the other hand, there are large discrepancies in the computation of the total mass of a CME with differences up to two orders of magnitude in the same event (as instance, see Stewart, 1974; Howard et al., 1985; Colaninno & Vourlidas, 2009; Vourlidas et al., 2010; Mishra et al., 2015). Therefore, it is possible to change this parameter in a wider range of values to improve the fit between the models and the observations at 1 AU.

It is worth to mention that we did not perform simulations varying the angular width (or the solid angle Ω) of the CME with the other input parameters fixed, due to the fact that the expelled mass $m = \dot{m} \Delta t \propto \Omega$, and therefore by varying Ω by a given percentage would result in the same profiles obtained by varying the same percentage but of the total mass (shown in Fig. 3). Moreover, variations of the solid angle less than 0.17 rad produce effects in the predicted profiles that can be neglected.

3.3 Models for different parameters of the solar wind

In order to investigate the dependence of the predicted density and velocity profiles at 1 AU with the initial conditions of the solar wind, we have performed numerical simulations varying the ejection velocity v_{SW} and the mass-loss rate \dot{m} of the wind. As a reference model, we have adopted $v_{\text{SW}} = 650 \text{ km s}^{-1}$, and $\dot{m} = 9.27 \times 10^{-15} M_{\odot} \text{ yr}^{-1}$. In these simulations we have fixed the CME parameters, assuming an ejection speed $v = 1330 \text{ km s}^{-1}$, and an expelled mass $m = 1.1 \times 10^{16} \text{ g}$, during an interval of time $\Delta t = 2.0 \text{ h}$. The resulting profiles are presented in Figure 4, in which the *black lines* depict the reference model.

First, we assume that the mass-loss rate of the pre-eruptive wind (Fig. 4: *panels a–b*), and the corresponding value of the post-eruption wind (Fig. 4: *panels c–d*), changes by $\pm 15\%$, $\pm 30\%$, $\pm 45\%$, $\pm 60\%$, and $\pm 75\%$, with respect to the reference parameter $\dot{m} = 9.27 \times 10^{-15} M_{\odot} \text{ yr}^{-1}$. The predicted density and velocity profiles at 1 AU are presented. The models with the lowest value of the mass-loss rate ($\dot{m} = 2.31 \times 10^{-15} M_{\odot} \text{ yr}^{-1}$) are depicted with *dark-red lines*, while the models with the highest value ($1.62 \times 10^{-14} M_{\odot} \text{ yr}^{-1}$) are shown with *light-orange lines*. We can see from *panel (a)* that longer transit times occur as the mass-loss rate of the pre-eruptive wind increases, as it is expected since the pre-eruptive wind slows the ejection. Besides, more extended compression regions and less-deep density drops are observed. In addition, it is observed in *panel (b)* that as lower is the mass-loss rate of the wind, stronger shocks arrive at Earth, as well as the detection of the shock wave and the rarefaction zone last for longer times. On the other hand, variations in the mass-loss rate of the post-eruption wind show that both the density and velocity profiles (*panels c–d*) are very similar in all models. Then, this parameter has no significant effect on the dynamics of the shock structure, that is, the travel time and speed of the leading shock are not modified. As it is expected, only the rarefied zone behind the compression region is affected.

Also, we compute numerical models assuming that the ejection velocity of the pre-eruptive wind (Fig. 4: *panels e–f*), and the corresponding speed of the post-eruption wind (Fig. 4: *panels g–h*), changes by $\pm 10\%$, $\pm 20\%$, $\pm 30\%$, $\pm 40\%$, and $\pm 50\%$ with respect to the reference value ($v_{\text{SW}} = 650 \text{ km s}^{-1}$). The models with the highest speed correspond to $v_{\text{SW}} = 950 \text{ km s}^{-1}$ (*light-green lines*), while those with the slowest speed correspond to $v_{\text{SW}} = 325 \text{ km s}^{-1}$ (*dark-green lines*). We note from the density profiles that as the pre-eruptive wind velocity decreases, the transit time of the leading shock is longer, as well as the compression region is more extended and the rarefied zone is denser. Moreover, the velocity profiles show stronger arrival shocks in the lower velocity models. On the

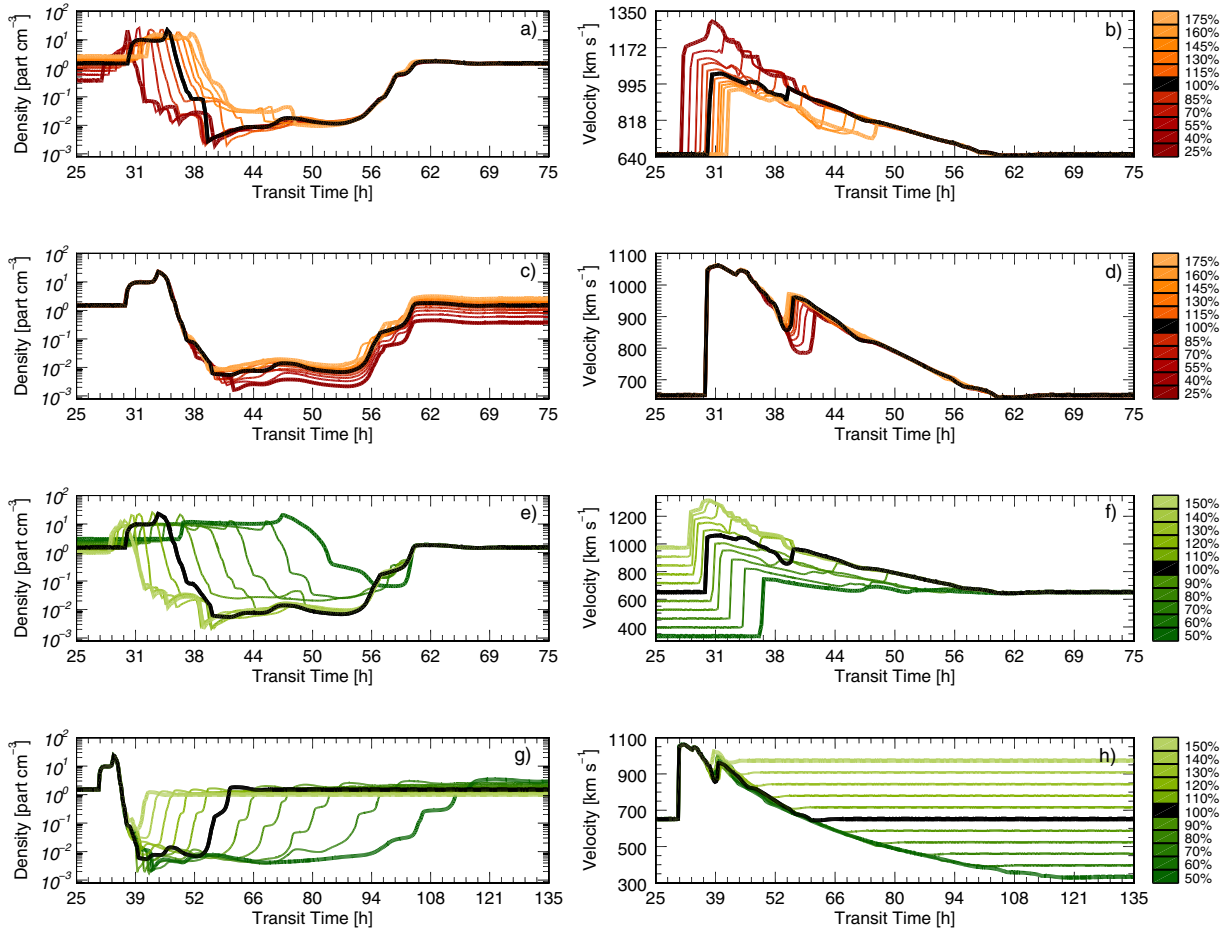


Fig. 4. Predicted density and velocity profiles as function of time for numerical models with different solar wind conditions (mass-loss rate \dot{m} , and ejection velocity v_{SW}). These models are computed allowing variations of one parameter, and letting the rest fixed. *Orange* profiles correspond to variations of \dot{m} of the pre-eruptive wind (*panels a–b*) and post-eruptive wind (*panels c–d*); and *green* profiles are obtained for different values of v_{SW} of the pre-eruptive wind (*panels e–f*), and post-eruptive wind (*panels g–h*). The variations of each parameter are shown by the color bars at the right side of the figure. The reference models are depicted with *black lines*, corresponding to a solar wind with $v_{\text{SW}} = 650 \text{ km s}^{-1}$ and $\dot{m} = 9.27 \times 10^{-15} M_{\odot} \text{ yr}^{-1}$. The detailed description of the figure is given in the text.

other hand, the resulting profiles from variations of the velocity of the post-eruption solar wind show that the compression region is not modified in these simulations, but obviously, the rarefaction zone is more extended in the lower-velocity models. Consequently, observations at 1 AU of the compression region duration, might not depend on the post-eruption solar wind conditions.

We note from our simulations that the density in the rarefaction zone reaches very low values. This is a limitation of our model, the density may reach higher values in this region whether the magnetic field is included.

3.4 Parametrization

Based on the previous exercise, we investigate possible correlations between the physical properties of the ICME at 1 AU and the injection parameters of the CME. Our results are summarized in [Figure 5](#), where we present (in percentage) the variations of the arrival velocity (*panel a*), the travel time (*panel b*), the total extension (*panel c*), the compression region

extension (*panel d*), the density enhancement (density variation found within the leading shock *panel e*), and the density drop (the difference between the minimum of density found within the rarefaction and the solar wind density value, *panel f*) of the ICME as function of the injection parameters of the CME.¹

¹ We call total extension, the interval of time in which the parameters of SW have changed, which includes the compression region and the rarefaction zone. The interval of time starts with the arrival at 1 AU of the leading shock and ends when the SW conditions resume again. This extension can be seen clearly in the velocity profile, with the arrival of the shocked structure driven by the ICME, when the speed suddenly increases and then, returns back to the SW speed. Whereas the compression region extension is the interval of time delimited by the increase of density. It starts with leading shock and ends when this parameter returns to the value of the ambient solar wind. The density enhancement corresponds to the density jump found within the leading shock while the density drop corresponds to the difference between the minimum of density found within the rarefaction and the solar wind density value.

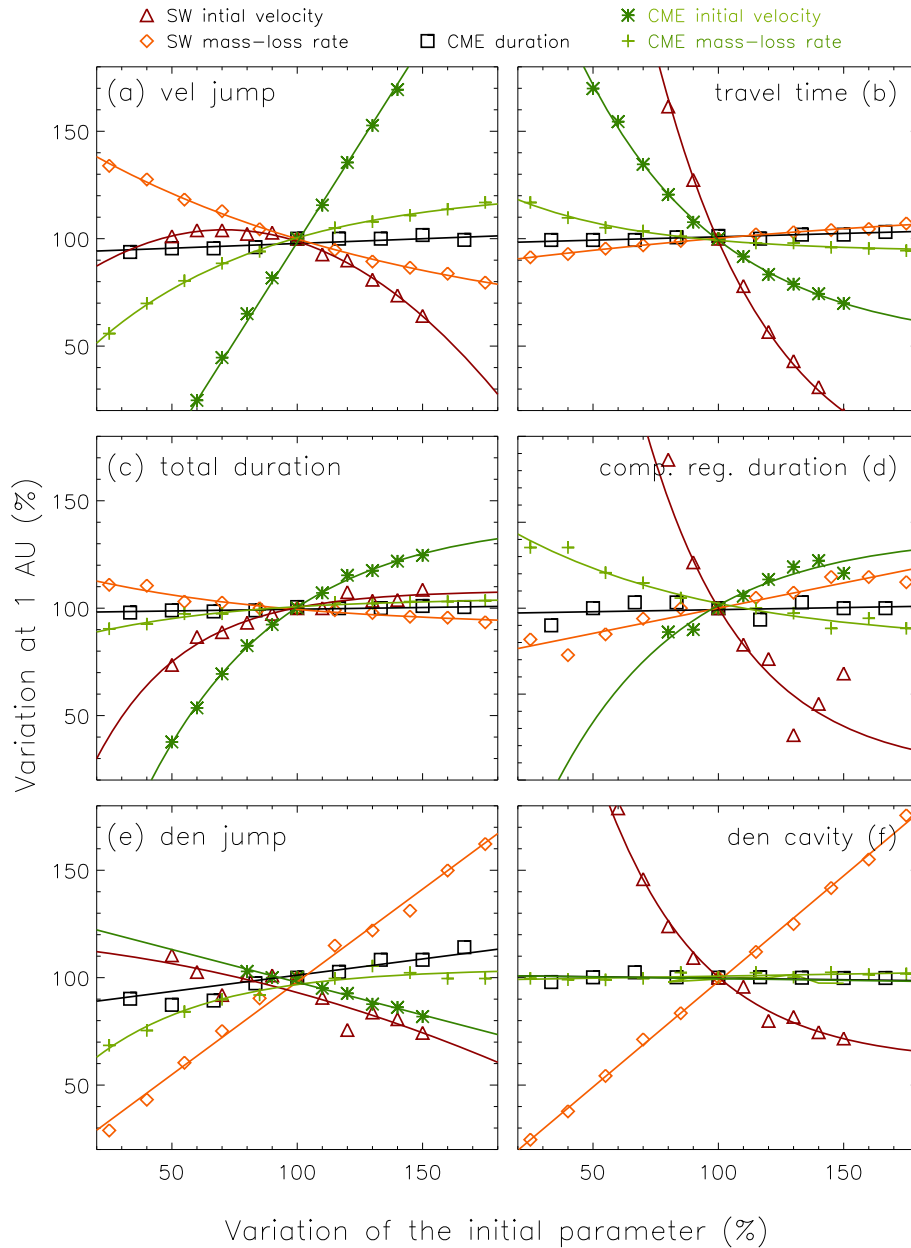


Fig. 5. Numerical results of the ICME structure at 1 AU as function of the initial parameters. Percentages of variation of arrival velocity (*panel a*), travel time (*panel b*), total extension (shock, compression region and the rarefaction zone; *panel c*), compression region extension (*panel d*), density jump at the shock front (*panel e*), and density drop in the rarefied zone (*panel f*) are presented. Percentage changes as function of the CME injection parameters are shown with *green solid lines*. The star symbols connected with *dark-green solid lines* are those changes obtained with the variation of the CME speed while plus symbols connected with *light-green solid lines* to those related to the CME mass-loss rate. Square symbols connected with *black solid lines* show the results obtained by changing the duration of the CME. Those changes related to the SW input parameters are shown in *red solid lines*: triangles connected with *dark-red solid lines* for the SW initial speed, and diamonds connected with *orange solid line* for the SW mass-loss rate.

In the figure, those symbols connected by *red/orange solid lines* correspond to variations of the initial solar wind parameters: triangles with *dark-red solid lines* refer to the SW initial velocity while diamonds with *orange solid lines* to the SW mass-loss rate. We show in *green solid lines* the variations of the CME parameters: stars with *dark-green solid lines* the CME initial speed and plus symbols with *light-green solid lines*

the CME mass-loss rate. *Black square* symbols connected by *solid lines* represent variations of the CME duration.

Important features can be seen in the figure. We note first that the CME duration has no significant effect on the arrival parameters of the ICME, and consequently, the *black solid lines* are roughly flat in all *panels*. This happens because the total mass of the CME and speed remained fixed for all the

simulations in which the duration time was changed, therefore, the total momentum is the same for all cases.

When possible, we have fitted analytic expressions to the relationship between CME and ICME variations in percentage. The variations of the arrival velocity depend on changes of the CME parameters (speed and mass-loss rate, *panel a*) as $\Delta v_{\text{ARR}} = -86 + 2\Delta v$, and $\Delta v_{\text{ARR}} = 123 - 95 \exp(-0.014 \Delta \dot{m})$, respectively, where the mass-loss rate of the CME is defined as $\dot{m} \equiv m/\Delta t$. On the other hand, by varying the solar wind conditions, we found: $\Delta v = 71 + \Delta v_{\text{SW}} - 0.01 \Delta v_{\text{SW}}^2$, and $\Delta v = 53 + 99 \exp(-0.007 \Delta \dot{m}_{\text{SW}})$. It is noteworthy that there is an asymptotic behavior of the arrival velocity with a limit of $\sim 23\%$ when the CME mass increases. For the travel time (*panel b*), we found that it is more affected by variations of the injected velocity of both the solar wind, $\Delta TT = -19 + 1087 \exp(-0.022 \Delta v_{\text{SW}})$; and the CME, $\Delta TT = 50 + 300 \exp(-0.0180 \Delta v)$.

The total extension of the ICME structure t_{EXT} (*panel c*) is a function of v and v_{SW} as $\Delta t_{\text{EXT}} = 142 - 265 \exp(-0.018 \Delta v)$, and $\Delta t_{\text{EXT}} = 108 - 138 \exp(-0.028 \Delta v_{\text{SW}})$, with asymptotic values of 42% and 8%, respectively. The compression region extension s_{EXT} (*panel d*) is more influenced by v_{SW} and \dot{m} as: $\Delta s_{\text{EXT}} = 4 + 1206 \exp(-0.025 \Delta v_{\text{SW}})$, and $\Delta s_{\text{EXT}} = 79 + 82 \exp(-0.012 \Delta \dot{m})$. Furthermore, we found that the density jump n_{J} (*panel e*), when the shock front arrives at 1 AU, depends on the variations of the solar wind conditions as: $\Delta n_{\text{J}} = 12 + 0.8 \Delta \dot{m}_{\text{SW}}$, and $\Delta n_{\text{J}} = 115 - 0.1 \Delta v_{\text{SW}} - 0.001 \Delta v_{\text{SW}}^2$. For the CME parameters, a good fit between the injection speed and the density jump is given by $\Delta n_{\text{J}} = 128 - 0.3 \Delta v$. It is interesting that the density jump is not affected at higher values of the expelled mass of CME. Finally, the density drop n_{D} in the rarefied zone depends on the solar wind parameters as $\Delta n_{\text{D}} = -0.05 + \Delta \dot{m}_{\text{SW}}$, $\Delta n_{\text{D}} = 500 \exp(0.025 \Delta v_{\text{SW}}) + 60$, but no dependence with the injection parameters of the CME is obtained from the simulations.

In summary, this behavior may be explained by the time evolution of the interacting surface, specifically, by the transfer of momentum between the CME and the SW ahead. Taking into account that the compression region is formed by both: the CME as well as the piled up SW materials, its temporal evolution (at a given heliospheric distance) depends on how fast the moment has been transferred from the CME to the SW material. If this transfer is slow the compression region will remain compact and if it is fast it will remain for a longer time. On the other hand, when the initial conditions allow a fast transfer of moment, the compression region will be smooth and wider.

This scenario is supported by the following points: As the mass (and therefore the momentum) of the CME increases, the compression region conserves its structure for longer time and distance, appearing at 1 AU as a compact and fast compression region. For a given distance, this structure loses compactness as the initial CME mass (and momentum) decreases (*Fig. 3a and b*). In similar way, when the density of the obstacle decreases, the transfer of moment is slower and the compression region is compact and fast whereas the transfer of moment is faster when the density of the obstacle increases causing a slower and wider compression region (*Fig. 4a and b*).

At sufficiently large distances (1 AU in our case), differences of the CME injection time are not important. This is

Table 2. Summary of the behavior (direct or inverse) of the speed and density jumps, the compression region duration and the travel time with the initial conditions of the CME and SW flows (mass-loss rate and speed).

	Direct	Inverse
Velocity jump	$v_{\text{CME}}, \dot{m}_{\text{CME}}$	$v_{\text{SW}}, \dot{m}_{\text{SW}}$
Density jump	$\dot{m}_{\text{CME}}, \dot{m}_{\text{SW}}$	$v_{\text{CME}}, v_{\text{SW}}$
Compression region duration	$v_{\text{CME}}, \dot{m}_{\text{SW}}$	$v_{\text{SW}}, \dot{m}_{\text{CME}}$
Travel time	\dot{m}_{SW}	$v_{\text{CME}}, v_{\text{SW}}, \dot{m}_{\text{CME}}$

due to the fact that the integrated CME momentum is the same independently of the injection time and therefore the interaction is similar (*Fig. 3c and d*). When the CME momentum increases due to an increase of velocity, the up-stream pile-up process dominates, causing an increase of the compression region width (*Fig. 3c and d*). This also is the case when the velocity of the pre-eruption SW decreases (*Fig. 4e and f*). The previous results combined with those on *Figure 5*, are summarized in *Table 2* which can be very useful to tune the simulated ICMEs temporal profiles in order to fit better the observations.

The ICME morphology is very important in terms of space weather. For instance, the compression region extension, speed and density jumps may be used to predict sudden storm commencement of geomagnetic storms (*Huttunen et al., 2005; Despirak et al., 2009*). Therefore, this exercise may help predict the effects of a CME at the Earth environment. Although, it is necessary to know the information of the magnetic field strength and polarity to predict the geomagnetic storm completely.

3.5 Comparison with observations

We apply the parametric study presented above in order to find the closest model to the *in situ* observations of the event of July 25, 2004. The ICME starting time was July 26, 2004 22:25 and the ending time was July 27, 2004 23:59 according to the Wind ICME Catalogue (http://wind.nasa.gov/index_WL_ICME_list.htm), corresponding to the ICME duration of 25.56 h.

In *Figure 6*, we show a comparison of the *in situ* data, obtained by WIND (from *top* to *bottom*), the magnetic field components (B_x , B_y and B_z), the magnitude of the magnetic field (B), the density (n) and the velocity (v) (in *black lines* for the last four) with the simulated profiles obtained with our model MEDIUM shown in *green lines* (see, *Table 1*) and our closest model to the observations depicted with the *amber line*. We have adopted the initial solar wind parameters $v_{\text{SW}} = 595 \text{ km s}^{-1}$ and $\dot{m}_{\text{SW}} = 1.28 \times 10^{-13} M_{\odot} \text{ yr}^{-1}$, obtained by reducing by $\sim 8\%$ and increasing by $\sim 50\%$ the original values of the model MEDIUM, respectively. We show the compression region duration and the rarefaction zone duration in *purple shades* for those times reported in the WIND ICME list. The compression region shown in *dark purple shade* is related to the CME sheath while the *light purple shade* corresponds to the ICME structure. We note that our model predicts a duration of 27.5 h (marked with the first and third *purple vertical solid*

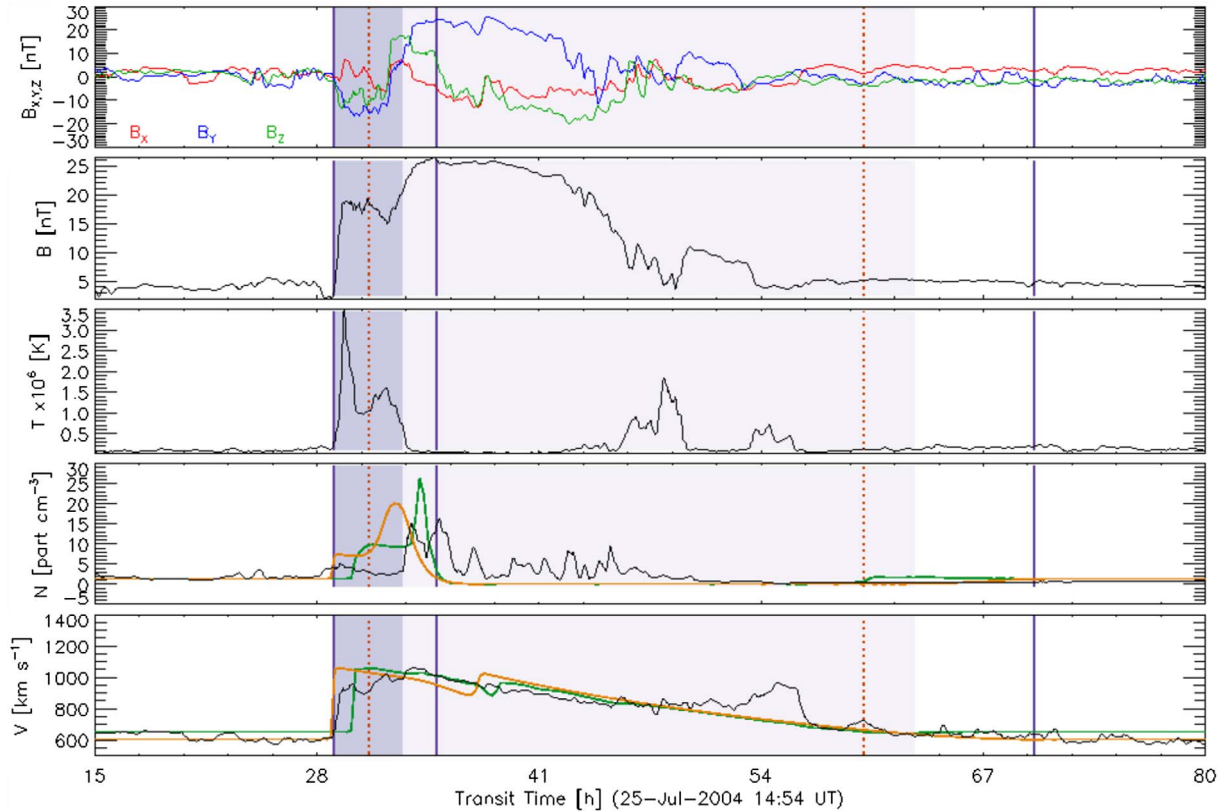


Fig. 6. Same as [Figure 2](#) but in this case, we included the simulated profiles obtained with the model MEDIUM (shown in *green line*) and our closest model model, in which we reduced the solar wind speed: +8% and increased the CME mass-loss rate $\sim 50\%$ (in *amber line*). The *in situ* data obtained by WIND are shown in *black lines* with a smooth of 15 min to make it comparable to our computational time-resolution. We have delimited in *purple vertical solid lines* our results for the duration of the compression region and the rarefaction zone. Whereas with *amber dotted lines* we have marked the end of the density plateau inside the compression region and the time in which the density return to the SW density value.

lines), that is, less than two hours of difference with the observed value. In terms of the duration of the compression region, our numerical model predicts a duration of 4.5 h (first and second *purple solid lines*), and then, we get a difference with observations of 1.7 h. In addition, we have a difference in the transit time $\Delta TT < 0.1$ h. Hence, our numerical results are in agreement with observations at 1 AU. Nevertheless, it is worth to mention that our predicted density profile, as well as the one obtained from the model MEDIUM, shows a rarefaction zone that is not consistent with observations.

This discrepancy between the predicted and observed profiles results from assuming the same conditions in both the pre-eruptive and post-eruption winds. However, it was shown in our parametric study, that the rarefaction zone is more extended as the velocity of the post-eruption wind decreases ([Fig. 3](#)). Therefore, the duration of the complete structure enlarges or shortens depending on the conditions of the post-eruption solar wind. This fact is very important to consider when characterizing the duration and structure of the ICMEs.

In [Figure 7](#), where the *amber line* represents the closest model to observation while in *red line* is plotted a new model in which the speed of the post-eruption solar wind has been

decreased to $v_{SW}^2 = 325 \text{ km s}^{-1}$. This results in a better fit on the duration of the rarefaction zone.

4 Numerical simulations of ICME–ICME interaction events

We studied three events (May 23, 2010; August 1, 2010; and November 9, 2012) on which two successive CMEs were launched in similar directions into the IPM. Using the model described in [Section 2](#), we investigate through numerical simulations the ICME–ICME interactions and their dynamical evolution.

With this numerical model, we obtain the density and speed profiles with a spatial and time resolution of 0.001 AU and 15 min, respectively. The code allow us to mark the different plasma structures involved in the interaction, namely: both ICMEs and the solar wind (prior, between, and after, the eruptions).

The ICME–ICME interaction can be identified by the appearing of a density peak caused by the plasma compression between the two ICMEs. As the interaction evolves, the density

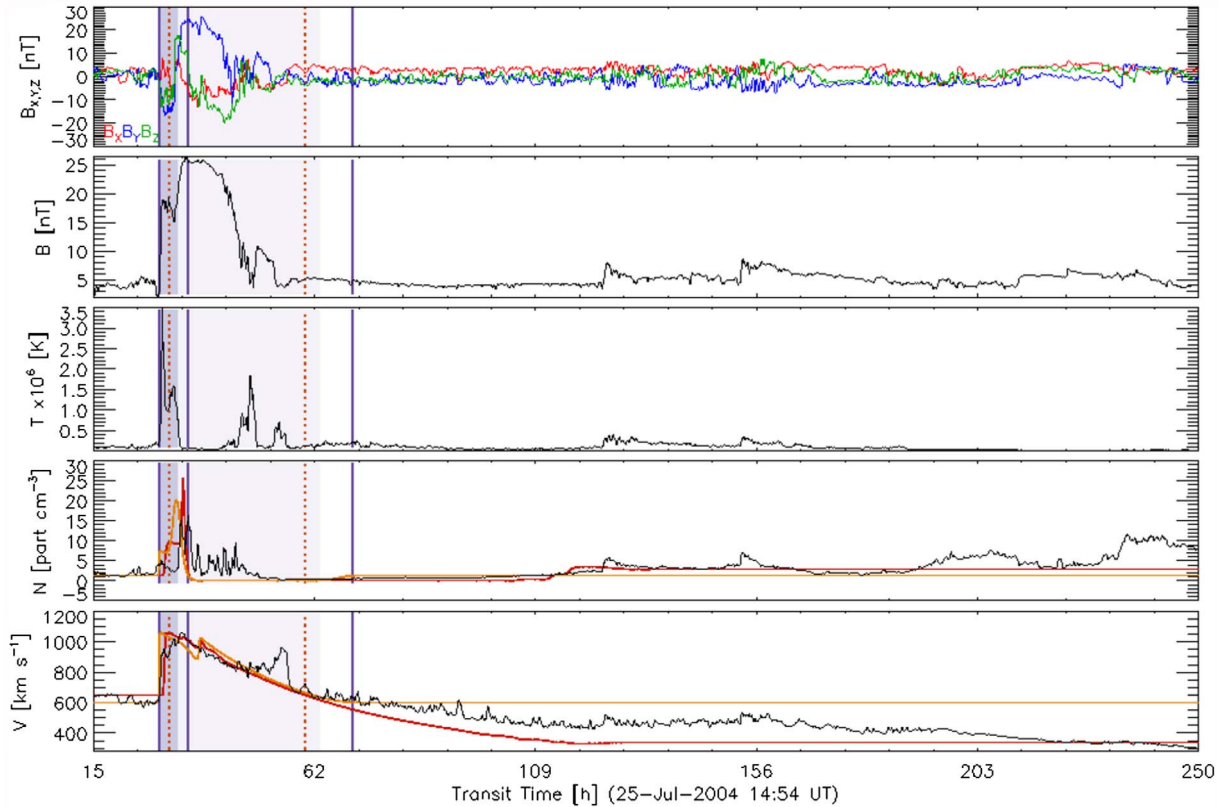


Fig. 7. Same as [Figures 2](#) and [6](#) but considering a longer time range. We have included the simulated profiles obtained with our closest model (shown in *amber*) while a model in which the post-eruption solar wind was slower down to $v_{\text{SW}}^2 = 325 \text{ km s}^{-1}$ (in *red*). It results in a better fit of the rarefaction zone. The *in situ* data obtained by WIND are shown in *black lines* with a smooth window of 15 min.

peak decreases and the time when this peaks is indistinguishable is considered as the time of the formation of the merged region. We find in the three events studied below that this time is comparable to the collision time reported by different authors.

4.1 Event of May 23, 2010

On May 23, 2010 at 18:06 UT, LASCO (on board of *SoHO* spacecraft; [Brueckner et al., 1995](#)) detected the first eruption (CME₁) with velocity $v_1 = 400 \text{ km s}^{-1}$, and total mass $m_1 = 1.5 \times 10^{16} \text{ g}$. The estimated duration of the eruption (from its brightness distribution; see [Lara et al., 2004](#)) was $\Delta t_1 = 2.85 \text{ h}$. Using these parameters, the computed mass-loss rate during the CME₁, within a solid angle $\Omega_1/4\pi \simeq 0.07$, is $\dot{m}_1 = 3.46 \times 10^{-13} \text{ M}_{\odot} \text{ yr}^{-1}$. The second eruption (CME₂) was observed by LASCO on May 24, 2010 14:06 UT, therefore, the interval of time between the two eruptions was $\Delta t_{\text{SW}} = 17.15 \text{ h}$. The velocity and the computed mass for this eruption are $v_2 = 650 \text{ km s}^{-1}$ and $m_2 = 1.0 \times 10^{16} \text{ g}$, respectively. We estimated a duration $\Delta t_2 = 3.71 \text{ h}$, and consequently, a mass-loss rate $\dot{m}_2 = 1.32 \times 10^{-13} \text{ M}_{\odot} \text{ yr}^{-1}$ within a solid angle $\Omega_2/4\pi \simeq 0.09$. For the solar wind, we have assumed a velocity $v_{\text{SW}} = 320 \text{ km s}^{-1}$ (that corresponds to the measured *in situ* value by WIND spacecraft on May 28, 2010 01:00 UT), and a mass-loss rate $\dot{m}_{\text{SW}} = 2 \times 10^{-14} \text{ M}_{\odot} \text{ yr}^{-1}$ ([Wood et al., 2002](#); [Cranmer, 2004](#)).

[Figure 8](#), shows the WIND spacecraft measurements (from *top to bottom*): B_x , B_y and B_z ; B , T , N , and V . The simulated profiles obtained with our numerical model using the input parameters described above are shown in *green lines* in the *last two panels*). We have shaded in *purple* the compression region duration and the rarefaction zone duration reported in the WIND ICME list while at the top in *orange* shades those reported by [Lugaz et al. \(2012\)](#). In *vertical red lines* we mark the duration of the compression region according to our second model (with *amber lines*).

As it was established in [Section 3.3](#), it is possible to better fit the observations by varying some of the initial conditions. Accordingly, we have reduced the CMEs mass-loss rates by 75% ($\dot{m}_1 = 8.65 \times 10^{-14}$, and $\dot{m}_2 = 3.3 \times 10^{-14}$); and the CMEs speeds by 20 km s^{-1} ($v_1 = 380 \text{ km s}^{-1}$ and $v_2 = 630 \text{ km s}^{-1}$). Assuming these changes, we obtain the profiles depicted with *amber lines* in the figure. With these changes, we achieved a difference between the observed and predicted arrival velocities $< 10 \text{ km s}^{-1}$, while the arrival density differs $< 10 \text{ cm}^{-3}$ with respect to the observed value. In our results and observations, the arrival density corresponds to the maximum value within the leading shock while the arrival speed as the maximum value within the compression region. In addition, we obtain a difference $< 0.1 \text{ h}$ for the travel time.

In order to understand the evolution of the interaction, in [Figure 9](#), we present the density (in *amber lines*) and velocity (in *black lines*) profiles, at the heliospheric distances

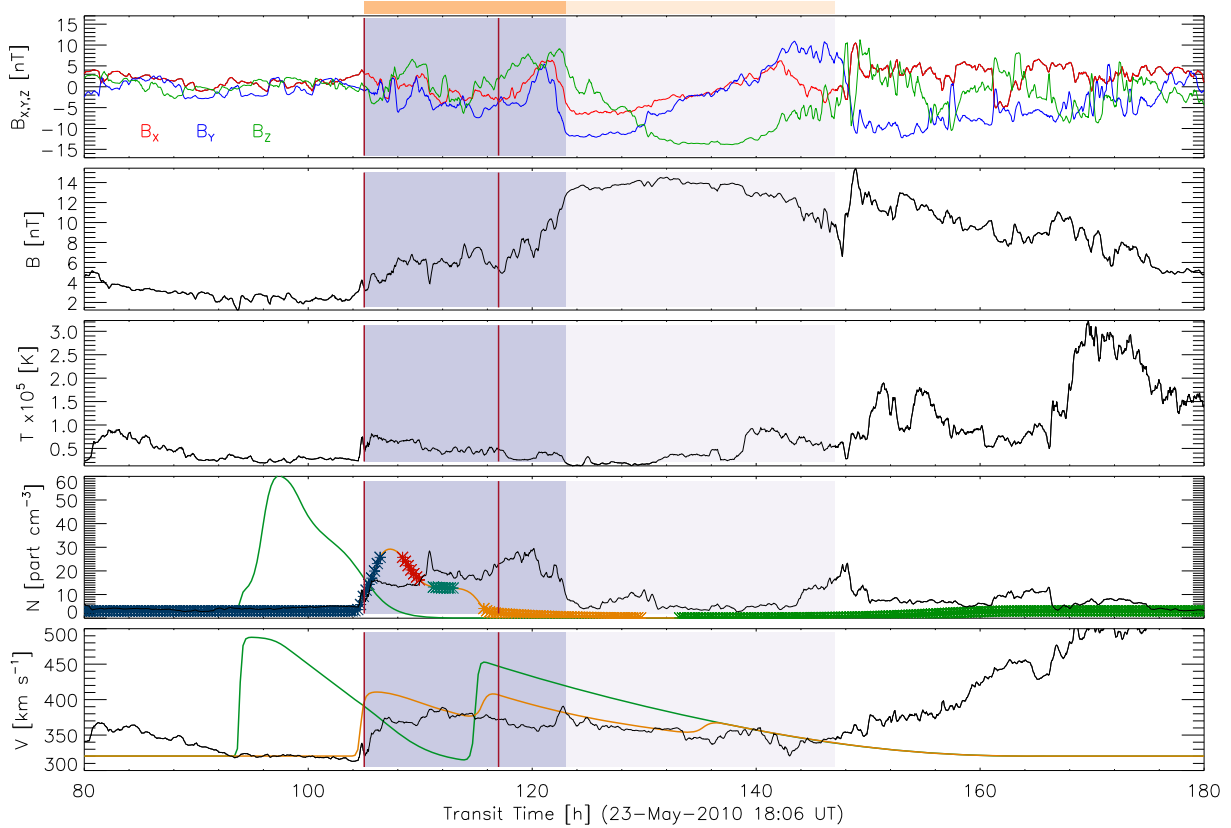


Fig. 8. Same as [Figure 2](#) but for the event of May 23, 2010. The numerical simulation assuming the reported parameters of the two CMEs corresponds to the *green line*, whereas the numerical model depicted with the *amber line* is obtained by reducing 75% the expelled mass during the eruptions, and 20 km s^{-1} the ejection velocities of the CMEs. We tag each plasma in the density profiles with colored crosses: the solar wind before CME₁ in *blue*, the CME₁ in *red*, the solar wind between the CMEs in *dark cyan*, the CME₂ in *amber* and the solar wind after the CME₂ in *green*. We have smoothed observations of the event with a running average of 15 min, in order to be consistent with the numerical simulations. Further description of the figure is given in the text.

$R = 0.1, 0.3, 0.5, 0.55, 0.6, 0.8$ and 1.0 AU (from *bottom to top*) predicted by our model for the event of May 23, 2010. In the figure, we have tagged with colored plus symbols, in the density profiles, the related plasma as follows: the pre-eruptive wind (in *blue*), the first CME (in *red*), the solar wind between the eruptions (in *aqua*), the second CME (in *amber*), and the post-eruption wind (in *green*). With shades, we mark the plasma related to the first ICME (in *red*), the second ICME (in *amber*) and the solar wind between both ICMEs (in *dark cyan*). At 0.55 AU , one can observe the development of a third density peak caused by the compression of the plasma between both ICMEs, showing that the interaction and the transfer of momentum between the ICMEs takes place. One can follow the evolution of the third peak between the ICMEs and that it appears and disappears as long as the interaction and transfer of momentum takes place. Once the merged region is formed the third peak completely disappears. For comparison with the analytic models we take as the interaction time (collision time), this time in which the merged region is formed.

It is noteworthy that the density and velocity profiles show the presence of a third shock behind the CME₂. This shock is produced from the interaction of the post-eruptive wind with the low-velocity material in the rarefaction zone (not with the

CME₂ itself), which is produced when the second eruption ends up, and the post-eruptive wind begins to be ejected. It is remarkable that this shock is weaker as it propagates into the IPM. This is a caveat of our HD model because this shock may be weaker or even disappear with the presence of normal component of the magnetic field that could inhibit the compression process.

We predict the ICME–ICME collision at a time $t \simeq 77.3 \text{ h}$ after the first CME is launched, and at a distance $R \simeq 0.8 \text{ AU}$ from the Sun. Beyond this distance, a single merged region is formed containing the material expelled during both eruptions. Afterwards, this region decelerates with time, reaching the Earth at a time $t_{\text{ARR}} \simeq 97.5 \text{ h}$, with an arrival speed $v_{\text{ARR}} = 417 \text{ km s}^{-1}$. These numerical results are consistent with the observed travel time of $\simeq 101 \text{ h}$, and the measured speed *in situ* of $\simeq 380 \text{ km s}^{-1}$ (see, for instance, [Lugaz et al., 2012](#)).

Through the analysis of the density and speed profiles variations, we were able to track the evolution of the interaction region. This is done by identifying the location of the maxima in each density and speed profiles which are obtained as function of time for different heliospheric distances.

Before the interaction, we identify two clear separate main maxima in the profiles corresponding to the two ICMEs. As the second ICME approaches the first one, the distance

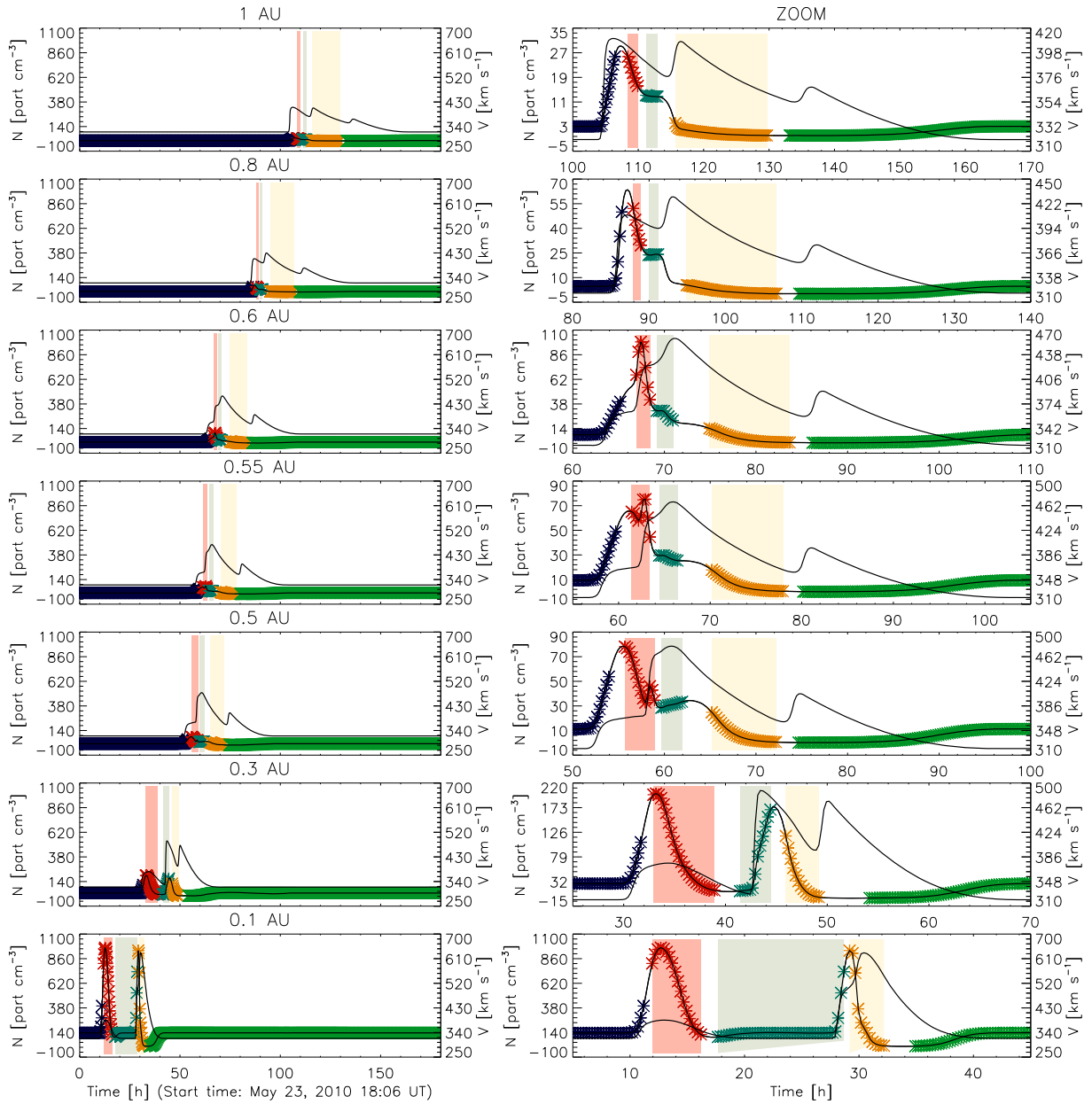


Fig. 9. Profiles of density (*star colored symbols*) and velocity (*black solid lines*) as function of time at different heliospheric distances (from *bottom to top*: 0.1 AU, 0.3 AU, 0.5 AU, 0.55 AU, 0.6 AU, 0.8 AU and 1.0 AU) for the event of May 23, 2010. In the *left panels* we present these profiles with fixed axes to see the evolution of the interaction process while in the *right panels* a zoom to these figures was applied to clearly notice the structures involved, their interaction, and their evolution up to 1 AU. We tag each plasma in the density profiles with *colored crosses*: the solar wind before CME₁ in *blue*, the CME₁ in *red*, the solar wind between the CMEs in *dark cyan*, the CME₂ in *amber* and the solar wind after the CME₂ in *green*. While the interaction process takes place, it is observed the development of a third density peak between both ICMEs (clearly observed at 0.55 AU). This peak appears and disappears while the process occurs. Once it disappears completely, the merged region is formed (this time is similar with those obtained analytically and reported by [Lugaz et al., 2012](#)).

between the two main maxima decreases. After the interaction sets in, sharp local maximum appeared between the ICMEs corresponding main maxima, as a result of compression of the plasma between the two structures. In this way, we assume that the interaction starts when the distance between the two main maxima and at least one density peak appears inside the region delimited by the two main maxima. The process

ends, when all mentioned structures merge into a single structure and the small local maximum disappears which is considered as the collision time.

Moreover, our numerical simulations are in good agreement with analytic results reported by [Niembro et al. \(2015\)](#) for the May 23, 2010 event. These authors predicted that the ICME–ICME interaction occurred at a time $\simeq 75.08$ h, and at

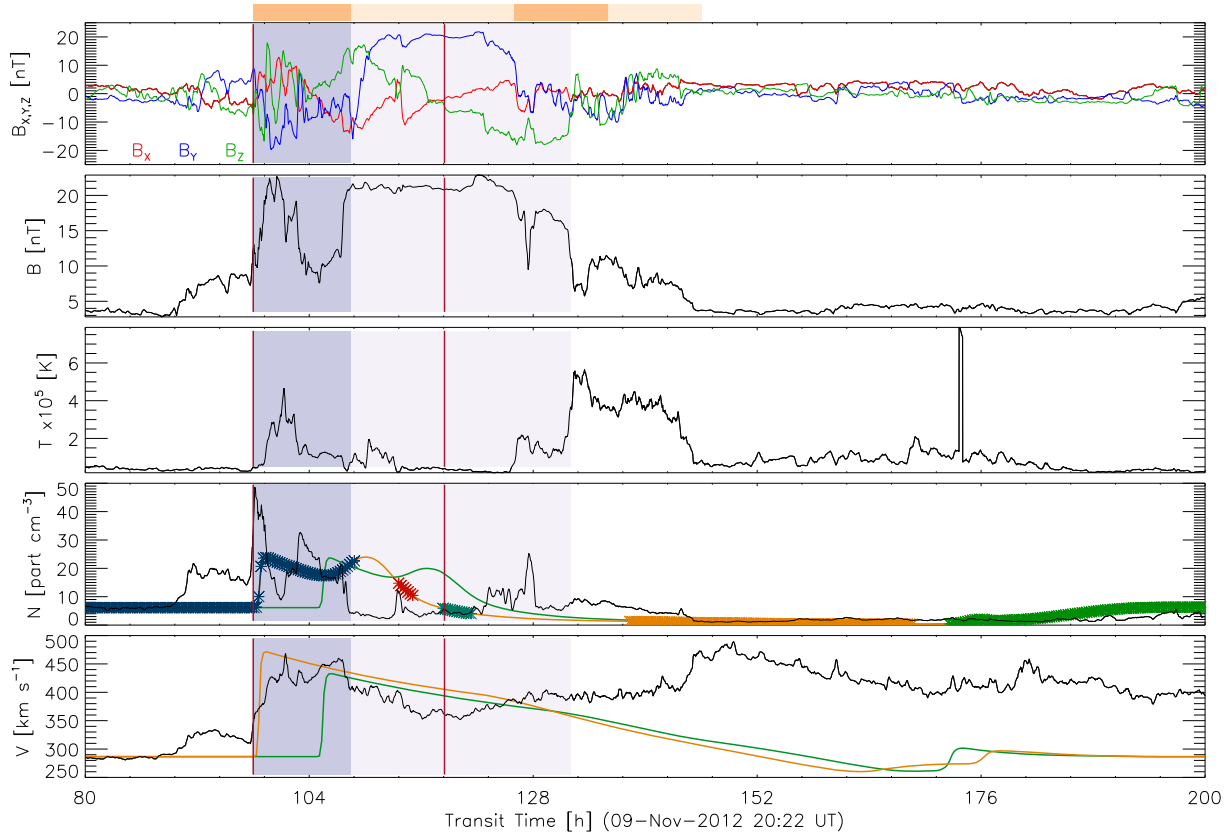


Fig. 10. Same as 8 but for the event of November 09, 2012. The simulated profiles with the original values are shown in *green* while those obtained by changing the mass-loss rate of the pre-eruptive wind (increased 20%), and the expelled mass of the CMEs 50%, and their speeds by adding 20 km s^{-1} (profiles shown in *amber* line in the *bottom* panels). In *purple* shades we show the compression region and rarefaction zone duration reported in the WIND ICME list while in *orange* shades those reported by Mishra et al. (2015).

a distance $\simeq 0.69 \text{ AU}$ from the Sun. Additionally, the predicted travel time and velocity of the merged region are $\simeq 105.2 \text{ h}$, and $\simeq 427 \text{ km s}^{-1}$, respectively.

We note that in Lugaz et al. (2012), it is argued that the CME₂ did not reach WIND spacecraft because of its deflection from the interaction with the CME₁. They stated that the density and velocity profiles observed are only due to the arrival of CME₁. Nevertheless, by assuming that both CMEs were ejected in the same direction and the deflection did not take place. A more detailed analysis of this event is required.

4.2 Event of November 9, 2012

On November 9, 2012 (see Mishra et al., 2015 for more details of this event), two successive earth-directed CMEs were launched and detected by *STEREO/SECHI* (Howard et al., 2008). The CME₁ was expelled from the Sun on November 9, 2012 at 17:39 UT, while the CME₂ was observed on November 10, 2012 at 06:39 UT. For CME₁, we assume that a mass of $m_1 = 4.66 \times 10^{15} \text{ g}$ was expelled during $\Delta t_1 \simeq 1.55 \text{ h}$, with a mean velocity of $v_1 = 500 \text{ km s}^{-1}$. The estimated mass-loss rate of the eruption is $\dot{m}_1 = 9.04 \times 10^{-14} \text{ M}_\odot \text{ yr}^{-1}$, within a solid angle $\Omega_1/4\pi = 0.14$. During the CME₂, a mass of $m_2 = 2.27 \times 10^{15} \text{ g}$ was expelled with a mean velocity of $v_2 = 1100 \text{ km s}^{-1}$. This second eruption last $\Delta t_2 \simeq 2.5 \text{ h}$,

obtaining a mass-loss rate of $\dot{m}_2 = 4.42 \times 10^{-14} \text{ M}_\odot \text{ yr}^{-1}$ within a solid angle $\Omega_2/4\pi = 0.09$. For the solar wind, we have adopted an ejection velocity $v_{\text{SW}} = 300 \text{ km s}^{-1}$ and a mass-loss rate $\dot{m}_{\text{SW}} = 1.5 \times 10^{-14} \text{ M}_\odot \text{ yr}^{-1}$.

In Figure 10, we present from *top* to *bottom* the WIND measurements: B_x , B_y , B_z , B , T , N , and V . We include the simulated density and speed profiles in the *bottom* two panels, respectively for two different models: using the original values described above (profiles shown with *green* lines) and with modified values (profiles shown with *amber* lines). The WIND spacecraft observations are smoothed by a running average of 15 min, which corresponds to our numerical time resolution. It can be seen from the figure that With the original initial values, the merged region reaches the Earth at a time 105 h (a difference with the observed travel time of more than 8 h), with a speed of 430 km s^{-1} , which differs only 15 km s^{-1} from the *in situ* data, and a density of 23 part cm^{-3} , that differs more than 10 part cm^{-3} .

Our closest model to observations (*amber* line) is obtained assuming a mass-loss rate of the solar wind $\dot{m}_{\text{SW}} = 1.8 \times 10^{-14} \text{ M}_\odot \text{ yr}^{-1}$, which is 20% higher than the original value. The mass-loss rates of the CME₁, and CME₂ are increased by 50%, thus $\dot{m}_1 = 1.356 \times 10^{-13} \text{ M}_\odot \text{ yr}^{-1}$, and $\dot{m}_2 = 6.63 \times 10^{-13} \text{ M}_\odot \text{ yr}^{-1}$, respectively. The initial CME velocities are also increased by 20 km s^{-1} . This model differs by 25 km s^{-1} ,

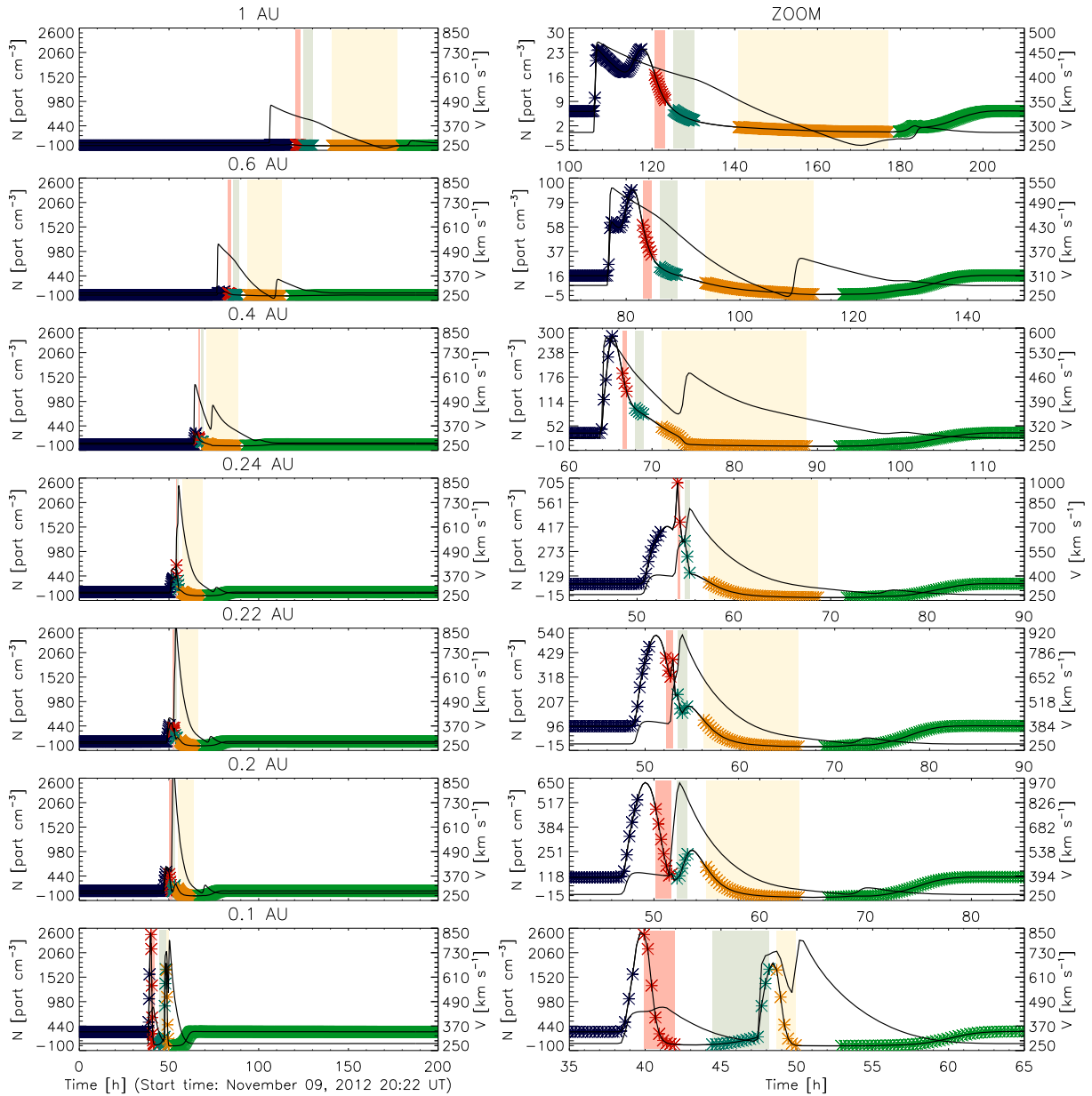


Fig. 11. Same as 9, but for the event of November 9, 2012. In this event, the interaction is predicted at a distance of $R \simeq 0.18$ AU, which corresponds to a time of $t \simeq 35$ h. The predicted travel time and velocity (at 1 AU) of the merged structure is 75 h after the first eruption, and 470 km s^{-1} , respectively.

and $<10 \text{ part cm}^{-3}$ with respect to the arrival velocity and density of the merged region. The travel time is exactly the same as the observations. In this figure, we shade in *purple* the compression region and rarefaction zone duration reported in the WIND ICME list while in *orange* shades those reported by Mishra et al. (2015). Their temporal locations differ significantly from our numerical simulation results.

In Figure 11 we show the predicted time-sequence of density (in *amber lines*) and velocity (in *black lines*) profiles for the event of November 9, 2012 at different heliospheric distances: 0.1 AU, 0.2 AU, 0.22 AU, 0.24 AU, 0.4 AU, 0.6 AU, and 1 AU. The simulation predicts that the ICME–ICME interaction starts at a time $\simeq 35$ h after the first eruption, at a heliospheric distance of $\simeq 0.18$ AU. Therefore, these results

differ from the observations (reported by Mishra et al., 2015) by 2 h, and 0.2 AU, respectively.

It is interesting to note that the evolution of the compression region after the interaction is completely different compared to the results obtained for the event of May 23, 2010 (shown in Fig. 9). The compression region evolves up to 1 AU forming two density peaks with same density values and both peaks are colored in blue, which tags the SW. In the previous event, the plasma colored in blue was retained near the leading shock, as the SW piles up in front of the structure. This behavior shows that the ICME–ICME interaction is a dynamic process which depends on the initial parameters and the time and distance where the observations of the merged region are performed.

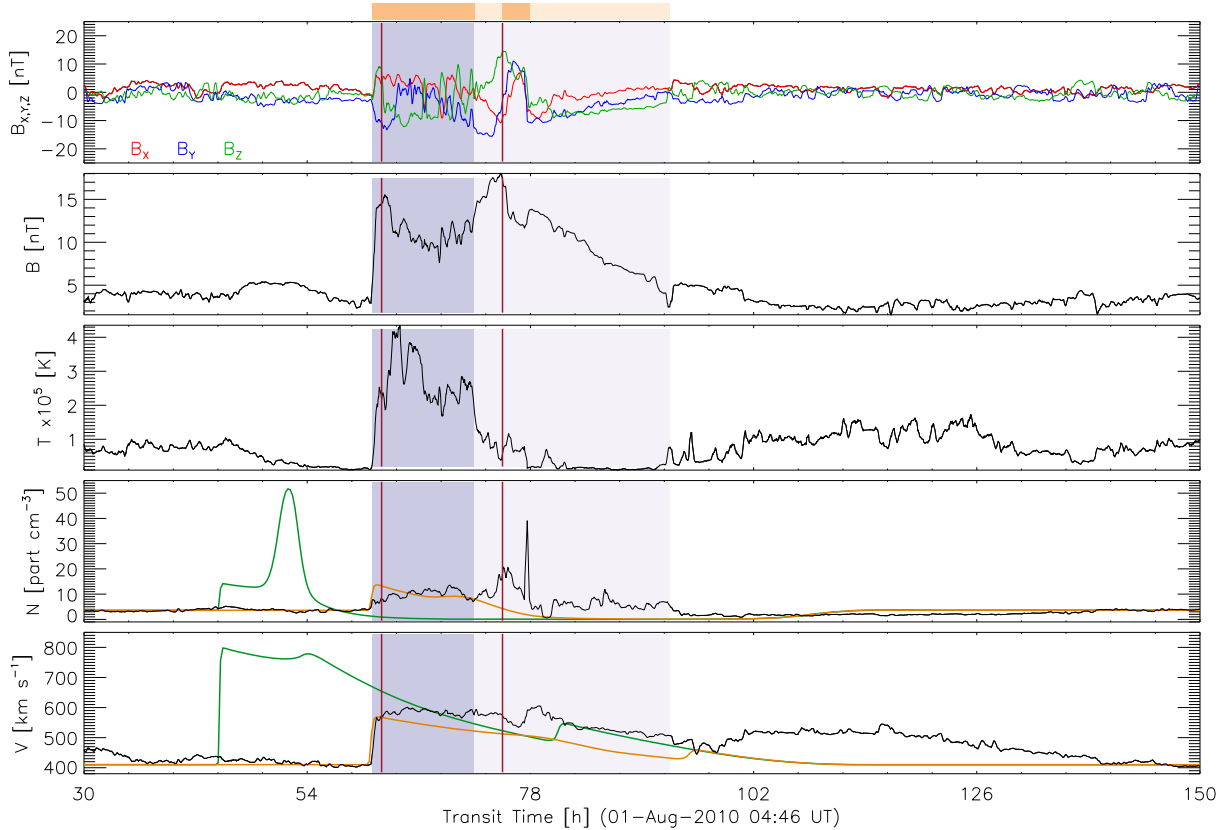


Fig. 12. Same as Figures 8 and 10, but for the event of August 01, 2010. The closest model (shown in *amber lines* in the *bottom two panels*) is obtained reducing less than 35% the mass-loss rate of the CMEs, and less than 5% their initial speeds. The description of the figure is given in the text.

This event was reported by Mishra et al. (2015), in which different components are identified within the arrival merged region at 1 AU: a shock front followed by a compression region, the CME₁, an Interaction Region and the CME₂. The Interaction Region is formed between both ICMEs and it is a result from the interaction between the ICMEs. Our simulation shows that the CME₂ ($v_2 = 1100 \text{ km s}^{-1}$) overtook the CME₁ ($v_1 = 500 \text{ km s}^{-1}$) at 0.18 AU (Fig. 11), making impossible the existence of the Interaction Region at 1 AU. This event is a good example of how difficult is the identification of the distinct components of complex regions.

The numerical results are consistent with observational values, as well as with analytic results reported by Niembro et al. (2015). The observations suggest that the collision occurred 19–36 h after the CME₁ was launched, at a distance of 0.16–0.46 AU. The observed travel time of the merged structure was $\simeq 96 \text{ h}$, with a velocity $\simeq 450 \text{ km s}^{-1}$. On the other hand, Niembro et al. (2015) predict that the CMEs collide at $\simeq 34.97 \text{ h}$, when they are located at a distance $\simeq 0.32 \text{ AU}$. In their models, the merged region arrives to the Earth $\simeq 99.23 \text{ h}$ after the first eruption, with a velocity of $\simeq 423 \text{ km s}^{-1}$.

4.3 Event of August 1, 2010

In the August 1, 2010 event, three successive CMEs were detected (e.g., Harrison et al., 2012; Liu et al., 2012; Temmer et al., 2012). Nevertheless, this event has been frequently

studied as the interaction of two consecutive CMEs. Here, we just consider the interaction between the last two ejections (here in after CME₁ and CME₂). The CME₁ was launched on August 1 2010 at 02:55 UT, with a speed of $v_1 = 732 \text{ km s}^{-1}$ during an interval of time of $\Delta t_1 \simeq 1.1 \text{ h}$ and a $m_1 = 8.0 \times 10^{15} \text{ g}$, that result in a mass-loss rate $\dot{m}_1 = 2.74 \times 10^{-13} M_{\odot} \text{ yr}^{-1}$, within a solid angle $\Omega_1/4\pi = 0.12$.

The CME₂ was launched from the Sun on August 1 at 7:45 UT, with the outflow parameters, $v_2 = 1138 \text{ km s}^{-1}$, and $m_2 = 3.0 \times 10^{16} \text{ g}$, within a solid angle $\Omega_2/4\pi = 0.18$. This eruption last $\Delta t_2 \simeq 1 \text{ h}$, and thus, $\dot{m}_2 = 7.39 \times 10^{-13} M_{\odot} \text{ yr}^{-1}$. For the solar wind, we assume an ejection velocity $v_{\text{SW}} = 410 \text{ km s}^{-1}$, and a mass-loss rate $\dot{m}_{\text{SW}} = 2 \times 10^{-14} M_{\odot} \text{ yr}^{-1}$ (see, for instance, Wood et al., 2002; Cranmer, 2004).

Figure 12 shows in the *bottom two panels* the predicted profiles of density and velocity using the original values (shown in *green lines*). Observations *in situ* by WIND spacecraft are also presented (*black line*), which are smoothed by intervals 15 min, as in the previous events. It can be seen in the figure that the numerical results are not consistent with observational data, since the travel time and velocity differs by more than 20 h and 200 km s^{-1} , respectively.

Our closest model model, shown in *amber lines* in the *bottom two panels* are obtained with the input parameters of the CMEs, $v_1 = 700 \text{ km s}^{-1}$, $v_2 = 1100 \text{ km s}^{-1}$, $\dot{m}_1 = 3.02 \times 10^{-13} M_{\odot} \text{ yr}^{-1}$, $\dot{m}_2 = 9.97 \times 10^{-13} M_{\odot} \text{ yr}^{-1}$. In this model, the arrival velocity differs by less than 5 km s^{-1} , whereas the

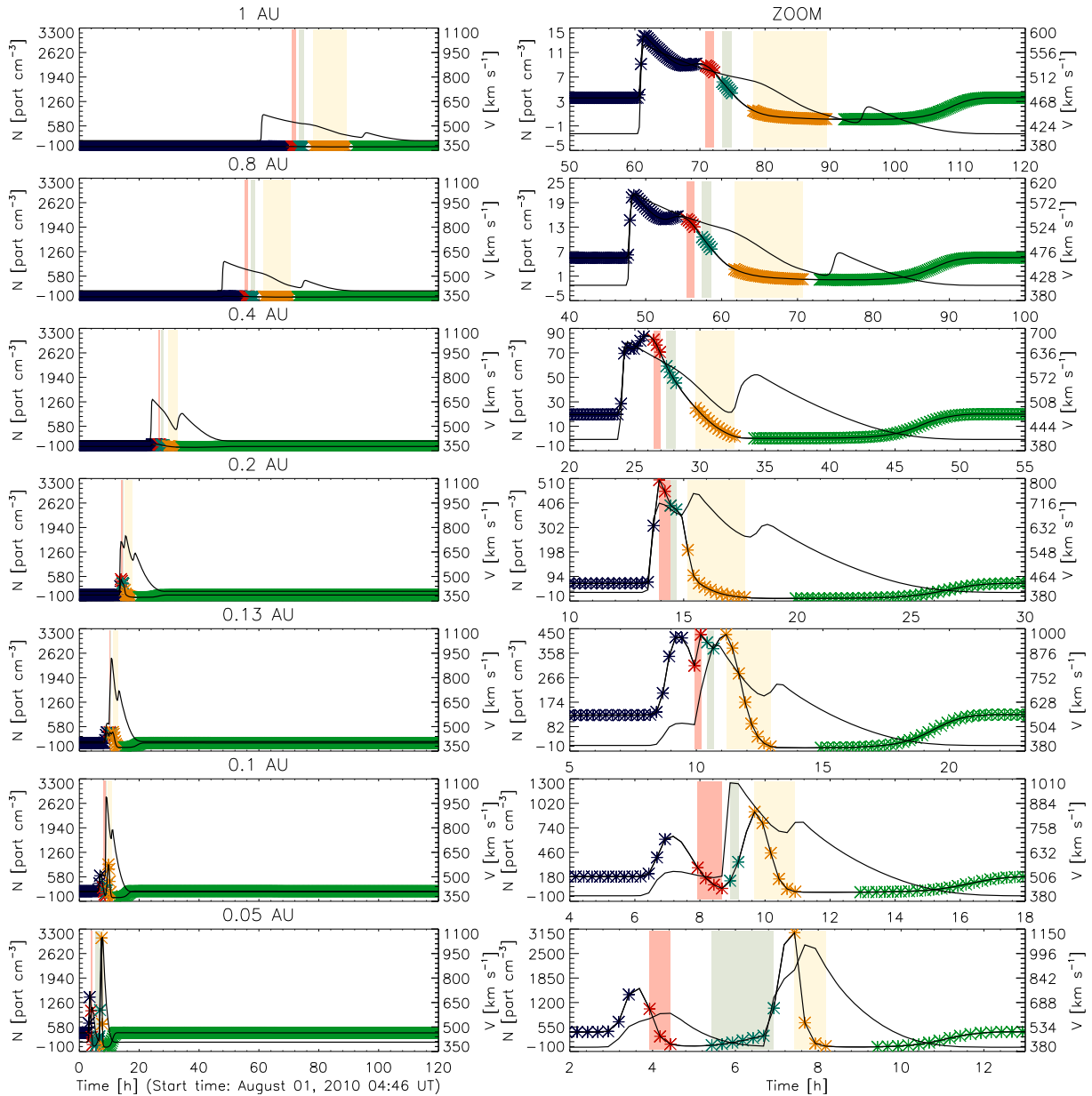


Fig. 13. Same as Figures 9 and 11, but for the event of August 01, 2010. In this event, the interaction is predicted at a distance of $R \simeq 0.19$ AU at a time $\simeq 15$ h after the first eruption. The merged region arrives to the Earth with a speed of 595 km s^{-1} , at an evolution time $\simeq 60.3$ h.

density difference is $\simeq 3 \text{ part cm}^{-3}$ with respect to the *in situ* data.

In Figure 13, we present a distance-sequence of density for the August 1, 2010 event. The density stratification at heliospheric distances $R = 0.05$ AU, 0.1 AU, 0.13 AU, 0.2 AU, 0.4 AU, 0.8 AU and 1.0 AU are shown. The numerical simulation predicts that ICME–ICME interaction occurs at a distance $\simeq 0.19$ AU, which corresponds to an evolution time $\simeq 15$ h after the first eruption. The merged region reaches the Earth with a speed of $\simeq 595 \text{ km s}^{-1}$, 60.3 h after the CME₁ is launched. We note that our numerical results are consistent with the observational data which suggest that the collision occurred at a time $\simeq 13$ h after the first eruption, at a

heliospheric distance $\simeq 0.16$ AU. Besides, the observed travel time of the merged region was $\simeq 60.3$ h, with a velocity $\simeq 600 \text{ km s}^{-1}$. In addition, Niembro et al. (2015) obtained similar results for this event. They showed that the CMEs collide at $\simeq 13$ h, when they are located at a distance $\simeq 0.2$ AU. Also, these authors computed a travel time of the merged region $\simeq 52.3$ h, with a velocity of $\simeq 726 \text{ km s}^{-1}$.

5 Conclusions

In order to study the dynamics, evolution and time profile at 1 AU of CMEs traveling into the IPM, as a function of the

initial conditions of both the ambient medium and the CME, we carried out a parametric study, using as reference the (single) CME event observed on July 25, 2004. By running numerical simulations varying the initial parameters, we found that the CME time duration has the lowest influence on the ICME time profile morphology, while the parameter with major influence on this profile is the CME velocity, followed by the CME mass-loss rate. This means that if we want to fit an observed ICME profile, we may vary the speed and/or the mass loss rate. Although, taking into account the observational uncertainties, we have ~20% of variation range over the speed, but we may vary the CME mass loss rate over a large range of values, because this is the parameter with the highest observational uncertainty. Then, varying these parameters, we were able to reproduce not only the travel time but the most important features of the speed and density profiles of our reference event.

In general, the compression region morphology depends on the pre-eruptive ambient solar wind and the CME parameters while the rarefaction zone structure depends on the CME parameters and the post-eruptive ambient solar wind conditions. With this in mind, we performed a simulation assuming a post-eruptive solar wind speed slower than the pre-eruptive one. It is clear that the rarefaction is due not only to the presence of the ICME, but the conditions of the post-eruptive solar wind are very important for its duration. Therefore, this effect should be considered when characterizing the duration of the ICMEs.

Commonly, the studies of the ICME transport focus in the accurate prediction of the travel time and arriving velocity and do not pay attention to the accuracy of the time profiles. Therefore, this parametric exercise is of utmost importance as it gives the relation of the speed and density profiles with the injection parameters, as well as clues of how the results of most of the hydrodynamic models can be improved by changing the CME mass-loss rate and/or the post-eruptive ambient solar wind conditions.

We use the results of our parametric study to simulate the CME interaction events detected and tracked as they rushed outwards into space on May 23, 2010; August 1, 2010; and November 9, 2012. The YGUAZÚ-A code used in our simulations, is able to tag the different flows involved in the interaction, i.e., the pre- and post-eruption ambient solar winds and both interacting CMEs. This is a good tool to analyze complex events and helps in its identification at 1 AU.

In summary, following our parametrization method, we found that the best results of the travel time (matching the exact time of the observations) were obtained, in general, by reducing the reported CME mass-loss rates. We found that our models can explain similarly the most important features of the speed and density profiles, and are able to distinguish, inside the merged region, the contribution of each of the interacting ICMEs. This study shows that the main characteristics of the ICME interaction can be obtained by studying the system hydrodynamically.

Acknowledgements. We would like to thank Alejandro Raga, Alejandro Esquivel and Pablo Velázquez for constructive discussions and all their helpful comments. We also would like to thank to Christophe Marquie, editor in charge, for all

his effort. The editor and us thank Pascal Demoulin and anonymous referee for their assistance in evaluating this paper. This work was partially supported by CONACyT grants 344896, and 179588; and UNAM/PAPIIT grants IN111716-3, IN112014, IN112116 and IG100516.

References

- Borgazzi A, Lara A, Echer E, Alves MV. 2009. Dynamics of coronal mass ejections in the interplanetary medium. *A&A* **498**: 885. DOI: [10.1051/0004-6361/200811171](https://doi.org/10.1051/0004-6361/200811171).
- Brueckner GE, Howard RA, Koomen MJ, Korendyke CM, Michels DJ, et al. 1995. The large angle spectroscopic coronagraph (LASCO). *Sol Phys* **162**: 357. DOI: [10.1007/BF00733434](https://doi.org/10.1007/BF00733434).
- Burlaga LF, Plunkett SP, St. Cyr OC. 2002. Successive CMEs and complex ejecta. *J Geophys Res* **107**: 1266. DOI: [10.1029/2001JA000255](https://doi.org/10.1029/2001JA000255).
- Burlaga L, Berdichevsky D, Gopalswamy N, Lepping R, Zurbuchen T. 2003. Merged interaction regions at 1 AU. *J Geophys Res* **108**: 1425. DOI: [10.1029/2003JA010088](https://doi.org/10.1029/2003JA010088).
- Cantó J, Gonzalez RF, Raga AC, de Gouveia Dal Pino EM, Lara A, González-Esparza JA. 2005. The dynamics of velocity fluctuations in the solar wind – I. Coronal mass ejections. *MNRAS* **357**: 572. DOI: [10.1111/j.1365-2966.2005.08670.x](https://doi.org/10.1111/j.1365-2966.2005.08670.x).
- Cargill PJ. 2004. On the aerodynamic drag force acting on interplanetary coronal mass ejections. *Sol Phys* **221**: 135. DOI: [10.1023/B:SOLA.0000033366.10725.a2](https://doi.org/10.1023/B:SOLA.0000033366.10725.a2).
- Chen J. 1996. Theory of prominence eruption and propagation: Interplanetary consequences. *J Geophys Res* **101**: 27499. DOI: [10.1029/96JA02644](https://doi.org/10.1029/96JA02644).
- Colaninno RC, Vourlidas A. 2009. First determination of the true mass of coronal mass ejections: A novel approach to using the two STEREO viewpoints. *ApJ* **698**: 852. DOI: [10.1088/0004-637X/698/1/852](https://doi.org/10.1088/0004-637X/698/1/852).
- Cranmer SR. 2004. New views of the solar wind with the Lambert W function. *Am J Phys* **72**: 1397. DOI: [10.1119/1.1775242](https://doi.org/10.1119/1.1775242).
- Despirak IV, Lubchich AA, Yahnin AG, Kozelov BV, Biernat HK. 2009. Development of substorm bulges during different solar wind structures. *Ann Geophys* **27**: 1951. DOI: [10.5194/angeo-27-1951-2009](https://doi.org/10.5194/angeo-27-1951-2009).
- Falkenberg TV, Vršnak B, Taktakishvili A, Odstrcil D, MacNeice P, Hesse M. 2010. Investigations of the sensitivity of a coronal mass ejection model (ENLIL) to solar input parameters. *Space Weather* **8**: 6. DOI: [10.1029/2009SW000555](https://doi.org/10.1029/2009SW000555).
- González RF, de Gouveia Dal Pino EM, Raga AC, Velázquez PF. 2004a. Gasdynamical simulations of the large and little homunculus nebulae of carinae. *ApJ* **600**: L59. DOI: [10.1086/381390](https://doi.org/10.1086/381390).
- González RF, de Gouveia Dal Pino EM, Raga AC, Velázquez PF. 2004b. Numerical modeling of carinae bipolar outflows. *ApJ* **616**: 976. DOI: [10.1086/425112](https://doi.org/10.1086/425112).
- González RF, Villa AM, Gomez GC, de Gouveia Dal Pino EM, Raga AC, Cant J, Velázquez PF, de La Fuente E. 2010. Revisiting 2D numerical models for the 19th century outbursts of carinae. *MNRAS* **402**: 1141. DOI: [10.1111/j.1365-2966.2009.15950.x](https://doi.org/10.1111/j.1365-2966.2009.15950.x).
- González-Esparza JA, Lara A, Santillan A, Gopalswamy N. 2003. A numerical study on the evolution of CMEs and shocks in the interplanetary medium. *Solar Wind Ten* **679**: 206. DOI: [10.1063/1.1618578](https://doi.org/10.1063/1.1618578).
- Gopalswamy N. 2016. History and development of coronal mass ejections as a key player in solar terrestrial relationship. *Geosci Lett* **3**: 8. DOI: [10.1186/s40562-016-0039-2](https://doi.org/10.1186/s40562-016-0039-2).

- Gopalswamy N, Yashiro S, Kaiser ML, Howard RA, Bougeret J-L. 2001. Radio signatures of coronal mass ejection interaction: Coronal mass ejection cannibalism? *ApJ* **548**: L91. DOI: [10.1086/318939](https://doi.org/10.1086/318939).
- Harrison RA, Davies JA, Mostl C, Liu Y, Temmer M, et al. 2012. An Analysis of the origin and propagation of the multiple coronal mass ejections of 2010 August 1. *ApJ* **750**: 45. DOI: [10.1088/0004-637X/750/1/45](https://doi.org/10.1088/0004-637X/750/1/45).
- Howard RA, Sheeley NR Jr, Michels DJ, Koomen MJ. 1985. Coronal mass ejections: 1979–1981. *J Geophys Res* **90**: 8173. DOI: [10.1029/JA090iA09p08173](https://doi.org/10.1029/JA090iA09p08173).
- Howard RA, Moses JD, Vourlidas A, Newmark JS, Socker DG, et al. 2008. Sun earth connection coronal and heliospheric investigation (SECCHI). *SSR* **136**: 67. DOI: [10.1007/s11214-008-9341-4](https://doi.org/10.1007/s11214-008-9341-4).
- Huttunen KEJ, Schwenn R, Bothmer V, Koskinen HEJ. 2005. Properties and geoeffectiveness of magnetic clouds in the rising, maximum and early declining phases of solar cycle 23. *Ann Geophys* **23**: 625. DOI: [10.5194/angeo-23-625-2005](https://doi.org/10.5194/angeo-23-625-2005).
- Kay C, Opher M. 2015. The heliocentric distance where the deflections and rotations of solar coronal mass ejections occur. *ApJ* **811**: L36. DOI: [10.1088/2041-8205/811/2/L36](https://doi.org/10.1088/2041-8205/811/2/L36).
- Lara A, González-Esparza JA, Gopalswamy N. 2004. Characteristics of coronal mass ejections in the near Sun interplanetary space. *Geofis Int* **43**: 1.
- Lara A, Gopalswamy N, Xie H, Mendoza-Torres E, Prez-Erquez R, Michalek G. 2006. Are halo coronal mass ejections special events? *J Geophys Res* **111**: A6. DOI: [10.1029/2005JA011431](https://doi.org/10.1029/2005JA011431).
- Liu YD, Luhmann JG, Mostl C, Martínez-Oliveros JC, Bale SD, Lin RP, Harrison RA, Temmer M, Webb DF, Odstrcil D. 2012. Interactions between coronal mass ejections viewed in coordinated imaging and *in situ* observations. *ApJ* **746**: L15. DOI: [10.1088/2041-8205/746/2/L15](https://doi.org/10.1088/2041-8205/746/2/L15).
- Liu YD, Luhmann JG, Lugaz N, Möstl C, Davies JA, Bale SD, Lin RP. 2013. On Sun-to-Earth propagation of coronal mass ejections. *ApJ* **769**: 45. DOI: [10.1088/0004-637X/769/1/45](https://doi.org/10.1088/0004-637X/769/1/45).
- Lugaz N, Vourlidas A, Roussev II, Jacobs C, Manchester WB IV, Cohen O. 2008. The brightness of density structures at large solar elongation angles: What is being observed by STEREO SECCHI? *ApJ* **684**: L111. DOI: [10.1086/592217](https://doi.org/10.1086/592217).
- Lugaz N, Farrugia CJ, Davies JA, Roussev II, Temmer M. 2012. The deflection of the two interacting coronal mass ejections of 2010 May 23–24 as revealed by combined *in situ* measurements and heliospheric imaging. *ApJ* **759**: 68. DOI: [10.1088/0004-637X/759/1/68](https://doi.org/10.1088/0004-637X/759/1/68).
- Lugaz N, Farrugia CJ, Manchester WB IV, Schwadron N. 2013. The interaction of two coronal mass ejections: Influence of relative orientation. *ApJ* **778**: 20. DOI: [10.1088/0004-637X/778/1/20](https://doi.org/10.1088/0004-637X/778/1/20).
- Lugaz N, Temmer M, Wang Y, Farrugia CJ. 2017. The interaction of successive coronal mass ejections: A review. *Sol Phys* **292**: 64. DOI: [10.1007/s11207-017-1091-6](https://doi.org/10.1007/s11207-017-1091-6).
- Manchester WB, Kozyra JU, Lepri ST, Lavraud B. 2014. Simulation of magnetic cloud erosion during propagation. *J Geophys Res* **119**: 5449. DOI: [10.1002/2015JA021415](https://doi.org/10.1002/2015JA021415).
- Mihalas D. 1978. *Stellar atmospheres*, 2nd edn. W. H. Freeman and Co, San Francisco.
- Mishra W, Srivastava N, Chakrabarty D. 2015. Kinematics of interacting CMEs of 25 and 28 September 2012. *Sol Phys* **290**: 527. DOI: [10.1002/2015JA021415](https://doi.org/10.1002/2015JA021415).
- Niembro T, Cantó J, Lara A, Gonzalez RF. 2015. An analytical model of interplanetary coronal mass ejection interactions. *ApJ* **811**: 69. DOI: [10.1088/0004-637X/811/1/69](https://doi.org/10.1088/0004-637X/811/1/69).
- Nieves-Chinchilla T, Linton MG, Hidalgo MA, Vourlidas A, Savani NP, Szabo A, Farrugia C, Yu W. 2016. A circular-cylindrical flux-rope analytical model for magnetic clouds. *ApJ* **823**: 27. DOI: [10.3847/0004-637X/823/1/27](https://doi.org/10.3847/0004-637X/823/1/27).
- Nieves-Chinchilla T, Vourlidas A, Raymond JC, Linton MG, Al-haddad N, Savani NP, Szabo A, Hidalgo MA. 2018. Understanding the internal magnetic field configurations of ICMEs using more than 20 years of wind observations. *Sol Phys* **293**: 25. DOI: [10.1007/s11207-018-1247-z](https://doi.org/10.1007/s11207-018-1247-z).
- Odstrčil D, Pizzo VJ. 1999. Three-dimensional propagation of CMEs in a structured solar wind flow: 1. CME launched within the streamer belt. *J Geophys Res* **104**: 483. DOI: [10.1029/1998JA900019](https://doi.org/10.1029/1998JA900019).
- Owens MJ, Arge CN, Spence HE, Pembroke A. 2005. An event-based approach to validating solar wind speed predictions: High-speed enhancements in the Wang-Sheeley-Arge model. *J Geophys Res* **110**: A12. DOI: [10.1029/2005JA011343](https://doi.org/10.1029/2005JA011343).
- Pizzo VJ. 1985. Interplanetary shocks on the large scale – A retrospective on the last decade’s theoretical efforts. *Wash DC Am Geophys Union Geophys Monogr Ser* **35**: 51. DOI: [10.1029/GM035p0051](https://doi.org/10.1029/GM035p0051).
- Prise AJ, Harra LK, Matthews SA, Arridge CS, Achillesos N. 2015. Analysis of a coronal mass ejection and corotating interaction region as they travel from the Sun passing Venus, Earth, Mars, and Saturn. *J Geophys Res* **120**: 1566. DOI: [10.1002/2014JA020256](https://doi.org/10.1002/2014JA020256).
- Raga AC, Navarro-Gonzalez R, Villagran-Muniz M. 2000. A new, 3D adaptive grid code for astrophysical and geophysical gasdynamics. *Rev Mex Astron Astrofis* **36**: 67.
- Riley P, Linker JA, Lionello R, Mikic Z, Odstrcil D, et al. 2004. Fitting flux ropes to a global MHD solution: A comparison of techniques. *J Atmos Sol-Terr Phys* **66**: 15. DOI: [10.1016/j.jastp.2004.03.019](https://doi.org/10.1016/j.jastp.2004.03.019).
- Schwenn R, dal Lago A, Huttunen E, Gonzalez W. 2005. The association of CMEs their counterparts near the Earth. *Ann Geophys* **23**: 1033. DOI: [10.5194/angeo-23-1033-2005](https://doi.org/10.5194/angeo-23-1033-2005).
- Shen F, Feng XS, Wang Y, Wu ST, Song WB, Guo JP, Zhou YF. 2011. Three-dimensional MHD simulation of two coronal mass ejections’ propagation and interaction using a successive magnetized plasma blobs model. *J Geophys Res* **116**: A09103. DOI: [10.1029/2011JA016584](https://doi.org/10.1029/2011JA016584).
- Shen F, Shen C, Wang Y, Feng X, Xiang C. 2013. Could the collision of CMEs in the heliosphere be superelastic? Validation through three dimensional simulations. *Geophys Res Lett* **40**: 1457. DOI: [10.1002/grl.50336](https://doi.org/10.1002/grl.50336).
- Siscoe G, Odstrcil D. 2008. Ways in which ICME sheaths differ from magnetosheaths. *J Geophys Res* **113**: A00B07. DOI: [10.1029/2008JA013142](https://doi.org/10.1029/2008JA013142).
- Stewart P. 1974. Strong wave propagation in a magnetized plasma. *A&A* **34**: 463.
- Strong KT, Saba JLR, Haisch BM, Schmelz JT. 1999. *The many faces of the Sun: A summary of the results from NASA’s Solar Maximum Mission*. DOI: [10.1007/978-1-4612-1442-7](https://doi.org/10.1007/978-1-4612-1442-7).
- Temmer M, Rollett T, Mostl C, Veronig AM, Vršnak B, Odstrcil D. 2011. Influence of the ambient solar wind flow on the propagation behavior of interplanetary coronal mass ejections. *ApJ* **743**: 101. DOI: [10.1088/0004-637X/743/2/101](https://doi.org/10.1088/0004-637X/743/2/101).
- Temmer M, Vršnak B, Rollett T, Bein B, de Koning CA, et al. 2012. Characteristics of kinematics of a coronal mass ejection during the 2010 August 1 CME-CME interaction event. *ApJ* **749**: 57. DOI: [10.1088/0004-637X/749/1/57](https://doi.org/10.1088/0004-637X/749/1/57).
- Vourlidas A, Howard RA, Esfandiari E, Patsourakos S, Yashiro S, Michalek G. 2010. Comprehensive analysis of coronal mass ejection mass and energy properties over a full solar cycle. *ApJ* **722**: 2. DOI: [10.1088/0004-637X/722/2/1522](https://doi.org/10.1088/0004-637X/722/2/1522).

- Vršnak B. 2001. Dynamics of solar coronal eruptions. *J Geophys Res* **106**: A11. DOI: [10.1029/2000JA004007](https://doi.org/10.1029/2000JA004007).
- Vršnak B, Gopalswamy N. 2002. Influence of the aerodynamic drag on the motion of interplanetary ejecta. *J Geophys Res* **107**: 1019. DOI: [10.1029/2001JA000120](https://doi.org/10.1029/2001JA000120).
- Vršnak B, Ruždjak D, Sudar D, Gopalswamy N. 2004. Kinematics of coronal mass ejections between 2 and 30 solar radii. What can be learned about forces governing the eruption? *A&A* **423**: 717. DOI: [10.1051/0004-6361:20047169](https://doi.org/10.1051/0004-6361:20047169).
- Vršnak B, Zic T, Falkenberg TV, Mostl C, Vennerstrom S, Vrbanec D. 2010. The role of aerodynamic drag in propagation of interplanetary coronal mass ejections. *A&A* **512**: AA43. DOI: [10.1051/00046361/200913482](https://doi.org/10.1051/00046361/200913482).
- Vršnak B, Zic T, Vrbanec D, Temmer M, Rollett T, et al. 2013. Propagation of interplanetary coronal mass ejections: The Drag-Based model. *Sol Phys* **285**: 295. DOI: [10.1007/s11207-012-0035-4](https://doi.org/10.1007/s11207-012-0035-4).
- Vršnak B, Temmer M, Zic T, Taktakishvili A, Dumbovic M, Mostl C, Veronig AM, Mays ML, Odstreil D. 2014. Heliospheric propagation of coronal mass ejections: Comparison of numerical WSA-ENLIL+Cone model and Analytical Drag-based model. *ApJS* **213**: 21. DOI: [10.1088/0067-0049/213/2/21](https://doi.org/10.1088/0067-0049/213/2/21).
- Wood BE, Muller H-R, Zank GP, Linsky JL. 2002. Measured mass-loss rates of solar-like stars as a function of age and activity. *ApJ* **574**: 412. DOI: [10.1086/340797](https://doi.org/10.1086/340797).
- Xie H, Ofman L, Lawrence G. 2004. Multiple ions resonant heating and acceleration by Alfvén/cyclotron fluctuations in the corona and the solar wind. *J Geophys Res* **109**: A8. DOI: [10.1029/2004JA010501](https://doi.org/10.1029/2004JA010501).
- Xiong M, Zheng H, Wu ST, Wang Y, Wang S. 2007. Magnetohydrodynamic simulation of the interaction between two interplanetary magnetic clouds and its consequent geoeffectiveness. *J Geophys Res* **112**: A11. DOI: [10.1029/2007JA012320](https://doi.org/10.1029/2007JA012320).
- Yashiro S, Gopalswamy N, Michalek G, St. Cyr OC, Plunkett SP, Rich NB, Howard RA. 2004. A catalog of white light coronal mass ejections observed by the SOHO spacecraft. *J Geophys Res* **109**: A7. DOI: [10.1029/2003JA010282](https://doi.org/10.1029/2003JA010282).
- Zhao X, Dryer M. 2014. Current status of CME/shock arrival time prediction. *Space Weather* **12**: 448. DOI: [10.1002/2014SW001060](https://doi.org/10.1002/2014SW001060).

Cite this article as: Niembro T, Lara A, González RF & Cantó J 2019. Numerical simulations of ICME–ICME interactions. *J. Space Weather Space Clim.* **9**, A4.